TECHNISCHE UNIVERSITÄT WIEN

VIENNA UNIVERSITY OF TECHNOLOGY

DIPLOMARBEIT

High resolution functional retinal imaging

Ausgeführt am

Institut für Biomedizinische Technik und Physik

Bereich Medizinische Physik

Der Medizinischen Universität Wien

unter der Anleitung von

Univ. Prof. Dr. Rainer A. Leitgeb

unter der Mitwirkung des

Instituts für Angewandte Physik

Der Technischen Universität Wien

unter der Anleitung von

Univ. Prof. Dipl.-Ing. Dr.techn. Martin Gröschl

durch

Maria Gershteyn

Achauerstrasse 8/5/17, 2333 Leopoldsdorf bei Wien

Matrikelnummer: 1027245

(Datum)   (Unterschrift)

Kurzfassung

Diverse Studien und Untersuchungen haben gezeigt, dass viele häufig auftretenden Augenkrankheiten (z. B. Glaukoma) mit Veränderungen in der Nervenfaserschicht und mit Schädigung der Ganglionzellen in Zusammenhang gebracht werden können. Polarisationssensitive Optische Kohärenz Tomographie (PSOCT) als eine funktionelle Erweiterung von Fourier Domain Optische Kohärenz Tomographie (SDOCT), ermöglicht eine Kontrasterhöhung in den zuvor erwähnten Schichten und liefert dadurch zusätzliche Informationen für frühere Diagnostik von Netzhautkrankheiten. Das in dieser Arbeit verwendete PSOCT System benötigt nur eine einzige Kamera, da es auf der Modulation der räumlichen Frequenzen beruht. Dieses spezielle System wurde modifiziert um hochauflösende retinale Bildgebung zu ermöglichen, die mit Strahldurchmesser 9,5 µm auf der Retina durchgeführt wurde. Im Rahmen dieser Arbeit wurden die optimalen Parameter zur Durchführung einer erfolgreichen Messung wie z. B. Probenanzahl, Sampling-Faktor und Messzeit bestimmt. Die theoretischen Berechnungen wurden sowohl mit einem während des Projektes entwickelten Testobjektes, das die optischen Abbildungseigenschaften des Auges simuliert, als auch mit in vivo Messungen überprüft und bestätigt.

Abstract

Various studies have shown that many important eye disorders such as glaucoma are related to abnormalities in the retinal nerve fiber layer and ganglion cells diseases. Polarization Sensitive Optical Coherence Tomography (PSOCT) as an extension of Spectral Domain Optical Coherence Tomography (SDOCT) has proven to allow contrast enhancement of the layers of interest mentioned above and therefore to provide for more information helping in early diagnosis of the retinal disorders. A PSOCT system based on spectral frequency multiplexing using one camera as a detector was modified for high-resolution retinal imaging with a transverse spot size on the retina 9.5 μm. The investigation of optimal set of operational parameters for this PSOCT system such as number of samples, oversampling factor and measurement time was carried out and the parameters for optimal performance were defined. The theoretical calculations were proven by series of measurements both with a test target and *in vivo.*

Acknowledgments

I would like to thank:

Univ. Prof. Dr. Rainer Leitgeb for his supervision, his help, patience and tactfulness,

Dipl.-Ing. Dr.techn. Martin Gröschl for helping me to find this project and being so supportive and always ready to help,

PhD Tilman Schmoll for his explanations and a lot of help with troubleshooting even after he was no longer present in the lab,

PhD Branislav Grajciar for supplying me with all the necessary technical equipment along the way and for his good advices.

Contents

1 Introduction

Optical Coherence Tomography (OCT) is a rapidly developing imaging technique based on a principle of low coherence interferometry. OCT allows capturing cross-sectional images and 3D volumes of weakly backscattering tissue with micrometer resolution in real time being moreover non-invasive and contact free. Many medical application fields, such as ophthalmology, dermatology and endoscopy have benefited from OCT with the most commercially successful being ophthalmology. [1]

In the field of ophthalmology the method profits from the transparency of the eye tissue allowing performance of measurements on the cornea's and retina's fine structures and showing the best resolution and speed compared to any other existing three dimensional imaging technique. [2]. This makes OCT to be of a great importance for the early diagnostics of various eye diseases affecting fine structures the change of which can be observed with OCT's high resolution on the earliest stages of the disease. [3]

One of the functional extensions of the OCT, Polarization Sensitive Optical Coherence Tomography (PSOCT) has proven to provide additional important information especially for retinal diseases. [4]. PSOCT is detecting polarization properties of the sample and uses this information to enhance the contrast of OCT intensity images. [5] This contrast enhancement has been demonstrated to significantly facilitate the diagnostics of several ocular as well as vascular diseases and there is a theory that a PSOCT system might be of great advantage in diagnostics of in particular glaucoma by allowing enhancing the contrast on the retinal nerve fiber layer (RNFL) and Ganglion Cell Layer (GCL), which is associated with this disease. (See Chapter 2).

The aim of this master thesis was to determine the optimal parameters that would enable us to perform high resolution PSOCT imaging on the human retina for further investigation of the properties of the RNFL and GCL of the human retina. Those parameters were found and implemented on a PSOCT system capable of retrieving retardation on the sample using single spectrometer. The system was redesigned and prepared for high-resolution PSOCT imaging and the optimal parameters such as measurement speed, amount of A-scans per second and oversampling factor [6] were determined and the performance of the system was studied. The proof-of-principle measurements using a tape stack as a sample are provided and the results of the in vivo measurement carried out on human retina are also presented.

The software for post processing was developed, implemented and applied to the acquired measurements.

In this report the basics and principles relevant to the present work are firstly introduced in the Chapter 2. The theory of OCT, different types of OCT detection (time domain, spectral domain and its extension PSOCT) are presented. The resolution issues are discussed and the overview of anatomy and physiology of human eye is given. Additionally diseases of the human eye related to pathological changes of polarization maintaining tissues in the eye, diagnostics of which could be improved by high-resolution PSOCT are described.

In Chapter 3 the PSOCT system principle and implementation are described. The alignment procedures and modifications introduced are documented as well as the data acquisition and data processing procedures. The characteristics of the system, such as resolution and sensitivity are discussed.

In the last Chapter the results obtained for a designed test sample are presented and discussed. The measured characteristics of the final configuration of the setup are also reported. The measurements are concluded with an *in-vivo* PSOCT recording of the retina of a healthy volunteer by applying the optimal parameters as determined in the course of the master thesis. This chapter is followed by conclusion of this work.

2 Basics and Principles

2.1 Optical Coherence Tomography

Optical Coherence Tomography (OCT) is a non-invasive imaging technique which operational principle is based on low-coherence interferometry. By means of measuring the intensity of the light reflected from within the tissue it provides high-resolution cross-sectional images. [2]

A generic OCT system is schematically represented in Figure 2.1. A fiber optic coupler implementing a simple Michelson interferometer principle is splitting the light from a low-coherence light into 2 arms: a reference arm and a sample arm. In the reference arm the light exiting the reference fiber is incident upon a reference delay and is back reflected from a reference mirror into the same fiber. In the sample arm the light exciting the sample fiber is incident upon a scanning mechanism (typically controlled by a computer) which is focusing the beam on a sample and carrying out the scanning of the focused spot in one or two lateral directions. The backscattered light from the sample is redirected back through the same system into the same sample arm fiber and to the fiber coupler where it is mixed with the returning back reflected reference arm light. The combined light then interferes on the surface of the detector and the electronic signals received are processed into an axial scan (A-scan), which represents the depth-resolved reflectivity profile of the sample at a fixed lateral position of the scanning mechanism. Multiple A scans can be acquired by the scanning mechanism sweeping the focused beam position across the sample. The A-scans are later assembled in two-dimensional cross-sectional image of the sample termed a B-scan. The series of B-scans can be assembled into volumes; such as 3D information about the sample can be obtained. Many specialized scanning systems have been developed for the various applications of OCT imaging in microscopy, ophthalmology, dermatology, etc. [7]
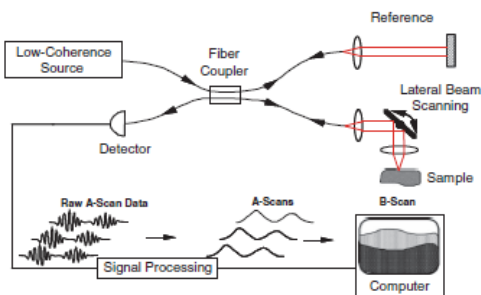

Figure 2.1: *A schematic representation of a generic OCT system. [7]*

2.1.1 Time-domain Optical Coherence Tomography

In Time Domain Optical Coherence Tomography (TDOCT) in order to record the interference signals from different reflection sites in depth the optical path length of the reference arm has to be matched to the corresponding scattering site of interest in the sample arm. (see Fig. 2.2) Thus the interference signal of different depth is being recorded as a function of time. [1] The light source in this case is low coherent, so that the interference is only observed when the sample and the reference path lengths are matched within the coherence length of the source, which therefore determines the axial resolution of the system.
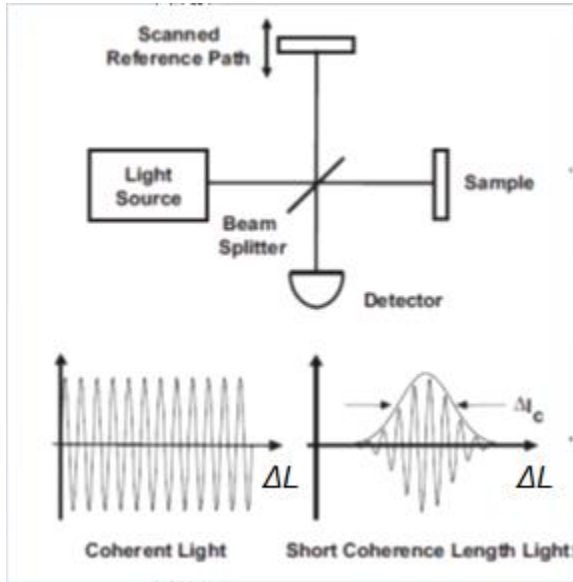

Figure 2.2: *A schematic representation of a TDOCT setup and principle of low-coherence interferometry. The light from the reference mirror and the sample arm interfere at the output of the Michelson interferometer. When the path difference ΔL between the electric field which travelled in the sample arm and the one that travelled in the reference arm is within the coherence length of the source Δl$_c$ the light interference is observed. [7]*

The intensity (I_0) of the electric field at the output of the interferometer measured at the detector is proportional to the square of the total field:

$$I_0 = |E_r|^2 + |E_s|^2 + 2E_r E_s \cos(2k\Delta L) \qquad\qquad (2.1)$$

Where:

$E_r(t)$ denotes a reference beam, $E_s(t)$ stands for the sample beam and ΔL is the path difference between the sample and the reference arms of the interferometer.

The used source is broadband and a single-channel photo receiver is used. [7]

The disadvantages of the TDOCT are the low sensitivity, and therefore slow acquisition speed and the necessity of the mechanical movement in the reference arm required to constantly match the optical path length.

Other, much faster techniques have been developed in which the detection is performed in Fourier domain rather than in time domain. [8]

2.1.2 Spectral Domain Optical Coherence Tomography

Spectral Domain Optical Coherence Tomography or Fourier Domain Optical Coherence Tomography (SDOCT or FDOCT) is an alternative method to TDOCT. SDOCT allows recording the interference signal for a complete depth scan instantaneously in the spectral domain, where the signal is acquired as a function of the wave number k.

 The interferometer design in comparison with TDOCT remains unchanged apart from the fact that the reference mirror is now fixed. In the same way as in TDOCT the output of the light source is split into two beams, one of which is directed into the tissue and back reflected or backscattered from it and the second one is reflected from a reference mirror. (Fig. 2.3) The sample beam and the reference beam have a relative time delay which is determined by the path length difference related to the depth of the structure in the sample. The interference of the two beams has a spectral modulation as a function of frequency which periodicity is reversely related to the echo time delay. The spectrometer equipped with a line scan camera captures the complete spectrum of the broadband light source once the light exits from the interferometer. The different echo delays which are producing different frequency modulations can be calculated by rescaling the spectrometer output from wavelength to frequency and then Fourier transforming the interference signal. As a result an A scan measurement of magnitude and echo delay of the light signal from the sample is obtained.
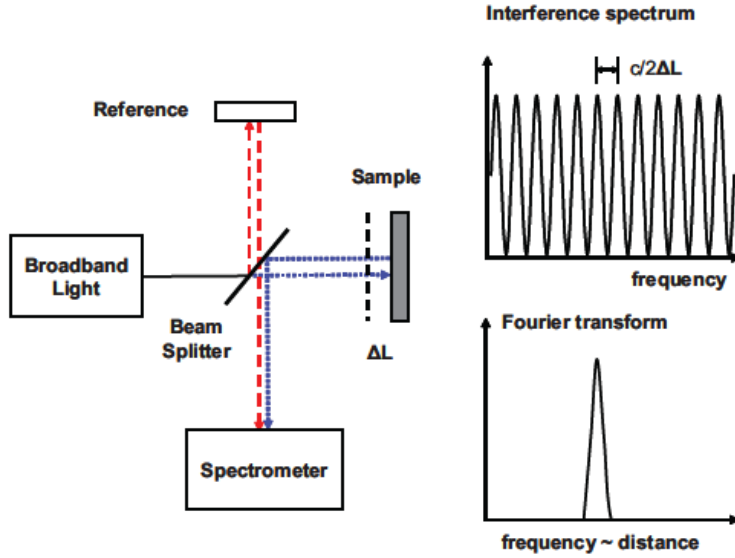
Figure 2.3: *Schematic representation of a SDOCT setup. The interference of the reference and sample beam contains spectral modulations of frequency due to path length difference or echo time delay. The axial scan information is obtained by a Fourier transformation. [7]*

In the processing stage while calculating the inverse Fourier transform of the spectral interference function 3 terms are created: a DC term, an auto-correlation term, and a cross-correlation term.

The DC term represents the intensities from the reference and sample arm. It is a constant offset and independent of the optical path difference. It can be significantly reduced by subtracting the measured spectrum of only the reference arm.

The auto-correlation term is caused by self-interference in the sample arm. The amplitude of it is however very small for the common case of the light intensity of the reference arm being much larger than the one from the sample arm and therefore can be neglected.

The cross-correlation term is depends on the optical path length difference of the reference arm and the sample arm and is proportional to the square root of the sample reflectivity. This leads to a significant sensitivity advantage of the method.

Whereas in TDOCT the maximum depth range is limited by absorption properties of the sample and the axial scanning range as well as axial resolution of the reference mirror the one of SDOCT is limited by the spectral resolution of the spectrometer.

The spectral resolution of the spectrometer is given as *δλ = Δλ/N* or *δk = Δk/N*, where *N* is the number of pixels used for sampling the spectral density function *S(k)*. [1] As the Nyquist theorem states that at least two sampling points are needed to resolve an oscillation the maximum depth range is to be calculated by:

$$\Delta z_{max} = \frac{\pi}{\delta k} \quad .$$

Using $\delta k = \frac{2\pi}{\lambda_0^2}\delta\lambda$ and δλ = Δλ/N, Δz_max can be written as [3]:

$$\Delta z_{max} = \frac{\lambda_0^2 N}{4\Delta\lambda} \quad . \tag{2.2}$$

With Δz_{max} being the maximum depth range, λ_0 central wavelength of the light source used, Δλ-full spectral range of it, *N* is the number of pixels used for sampling the spectral density function *S(k)*.

Significant advantage of the SDOCT comparing to the TDOCT is its higher sensitivity, which is the smallest sample reflectivity that an OCT system is able to resolve.This allows increasing the acquisition speed by several orders of magnitude without sacrificing the image quality. [8] Therefore it allows acquiring data with less motion artifacts and acquiring volumes of data within seconds.

2.1.3 Polarization Sensitive Optical Coherence Tomography

Polarization Sensitive Optical Coherence Tomography (PSOCT) is a functional extension of OCT which allows enhancing the contrast of the tissue with specific polarization maintaining or polarization altering characteristics which significantly facilitates the diagnostics of various diseases. [9,10]

A PSOCT system delivers a possibility to measure the polarization state of the backscattered light coming from the sample. Such quantitative properties of this light can be calculated as phase retardation and the fast optical axis orientation. In order to achieve those normally two spectral interferogramms, containing information on two orthogonally polarized light states, are acquired and processed. It is either implemented by illuminating the sample with light of different polarization states in time successively or simultaneously by means of two spectrometers [11]. Instrumentally it is implemented in a following way: At the entrance of interferometer the light is lineary polarized at 0°. Circular polarization of the light illuminating the sample is achieved by means of a quarter wave plate installed in front of the sample. The backscattered light is

generally elliptically polarized and depends on the birefringence of the sample. The quarter wave plate, oriented at 22.5°, installed at the reference arm acts as a half wave plate (because of the double pass) and rotates the vertically polarized light by 45°. The vertically polarized component of the reference arm light interferes with the vertical component of the backscattered light coming from the sample after the beam splitter as well as the horizontally polarized component interferes with the horizontal component of the backscattered light from the sample. After that those two orthogonal components are split by a polarizing beam splitter and the interferogramm of each of the polarization states is detected by one of the two corresponding spectrometers. Even though the parallel systems show better phase stability they are more complex due to the necessity of data synchronization and have higher price due to dual spectrometer design. [10]

The sample reflectivity *R(z)*, phase retardation *δ(z)* and the fast axis orientation *θ(z)* the amplitude and the phase of the complex valued signal after the Fourier transform of SDOCT are used [3]:

$$R(z) \propto A_1^2(z) + A_1^2(z) \quad , \tag{2.3}$$

$$\delta(z) = \arctan\left[\frac{A_2(z)}{A_1(z)}\right] \quad , \tag{2.4}$$

$$\theta(z) = \frac{\pi - \Delta\varphi(z)}{2} \quad , \tag{2.5}$$

Where *Δφ* is the phase difference between the two orthogonal polarization states.

2.1.4 Axial and transverse resolution in OCT

Because of the coherence gating in depth the decoupling of axial and transverse resolution in OCT takes place.

The axial (depth) resolution is only defined by the coherence length with is inverse proportional to the spectral bandwidth of the light source and is independent of the focusing optics. In order to define the axial resolution the coherence length of the round trip of the travelling light is used (light directed to the sample and the backscattered light from the sample), being half of the coherence length of the light source. The axial resolution for a source with Gaussian spectral distribution is therefore:

$$\delta z = \frac{l_{c_{FWHM}}}{2} = \frac{2ln2}{\pi}\frac{\lambda_0^2}{\Delta\lambda} \tag{2.6}$$

Where l_{cFWHM} is the coherence length of the light source,

λ_0 – is the center wavelength of the source,

$\Delta\lambda$ – the full width at half maximum (FWHM) of the central bandwidth of the source.

Hence it can be seen that in order to achieve high depth resolution either the central wavelength of the source has to be chosen smaller or the bandwidth increased. This however is conflicting with the goal to achieve high penetration, since longer wavelength scatters less and therefore penetrates deeper into the tissue the central wavelength has to stay reasonably high. Therefore the broadband sources are typically used.

The transverse resolution is limited by the spot diameter of the focused sample arm beam.

Using the diameter of the focused sample beam waist, the transverse resolution is defined by the lateral beam spot size:

$$\delta x = 2w_0 = 2\frac{\lambda_0}{\pi\,NA} \quad , \qquad\qquad (2.7)$$

Where w_0 is the beam waist, λ_0 the central wavelength and $NA \approx \frac{d}{2f}$ the numerical aperture of the focusing optics, where d is the diameter of the collimated beam and f is the focal length of the focusing optics.

The depth of focus (DOF) is proportional to the square of the lateral beam spot size δx and is defined as following:

$$DOF = \frac{\pi}{2\lambda_0}\delta x^2 \qquad\qquad (2.8)$$

Hence a tradeoff between the high transverse resolution and the DOF is a drawback of the ultra-high resolution OCT method in case isotropic resolution is needed. Using high NA allows achieving high transverse resolution but compromises the depth of focus of the OCT system. [3]

2.2. Anatomy and physiology of the human eye

Although the method exists only for about 20 years, OCT already plays a major role in clinical trials and practice for the management of retinal and cornea diseases of the human eye. [12]

This application of the OCT is mostly possible due to the transparent tissue of the eye, allowing good penetration. This method is widely used because it allows the creation of 3D tomograms of microscopic retinal structures, being the most convenient non-invasive technique existing for imaging in the eye.

Since this work is dedicated to the imaging of the human retina, a short overview of anatomy of human eye, retina and related diseases is given in the following section.

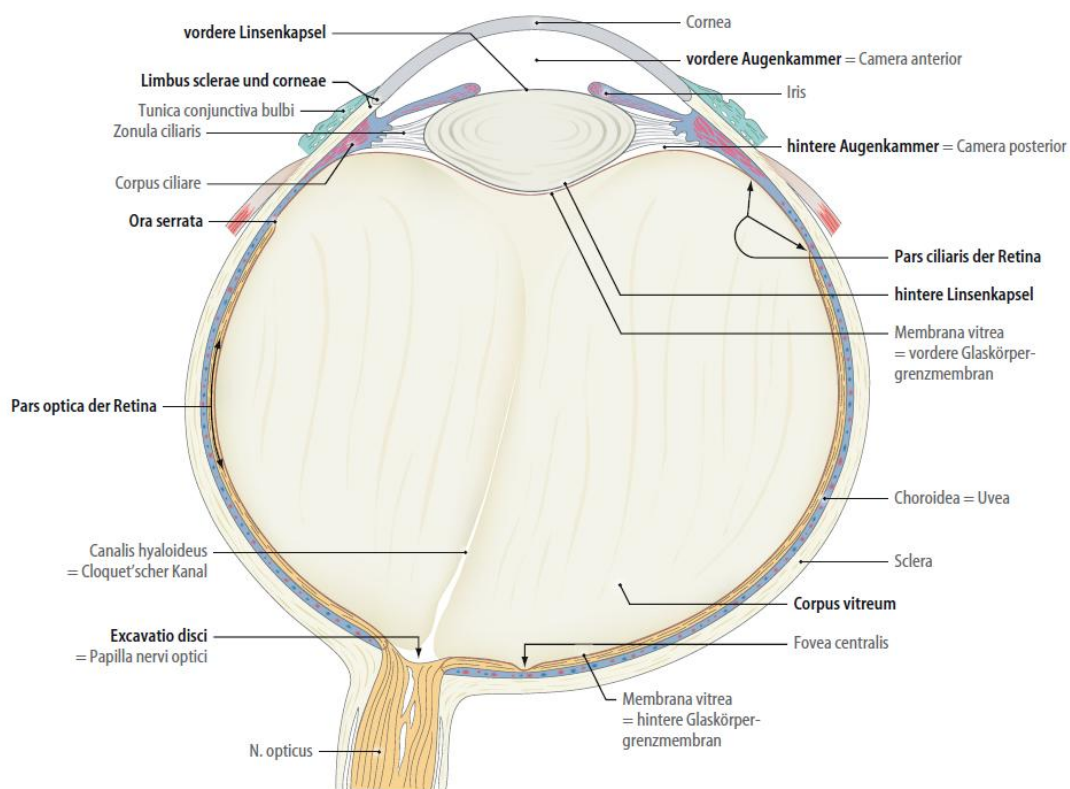### 2.2.1 Overview and structure of the human eye and retina

Figure 2.4: *a human eye (from [13])*

Fig. 2.4 illustrates a schematic drawing of the human eye ball. The physiology can be described as follows: The light enters the eye through the cornea, where it is refracted by the lens and

cornea itself. After travelling through the pupil and vitreous body the light is finally focused on the photoreceptors of the retina, where the chemical energy is then produced and transmitted into an electrical signal. The optic nerve transmits this signal to the part of the brain called optical cortex.

The focusing of the eye is mainly carried out by the cornea (with the refractive power of around 40 diopters) and the accommodating lens (around 20 diopters), with a total refractive power of around 60 diopters.

The lens, which is attached to the ligaments of the ciliary body, can be deformed, becoming more or less spherical, when they contract. Thus the focusing of the eye (which is by default in the relaxed state of the ligaments adjusted for viewing the objects in far distances) occurs.

2.2.2 Retina anatomy and physiology

The retina is the inner back surface of the eye. Its thickness varies from approximately 560µm in the center to 100µm on the periphery. The photoreceptors of the retina, responsible for the perception of light are called cones and rods. When exposed to light they produce chemical energy, which is, translated to electrical signal, afterwards transmitted to the optical cortex via the optic nerve. The rode cells (rods) (approximately 120 million) are responsible for the vision in dim light and black and white vision. The cones (cone cells) (6-7 million) have 3 different pigments with absorption maxima at the wavelength of 420nm (blue), 530 nm (green) and 560 nm (red). That enables the color vision.
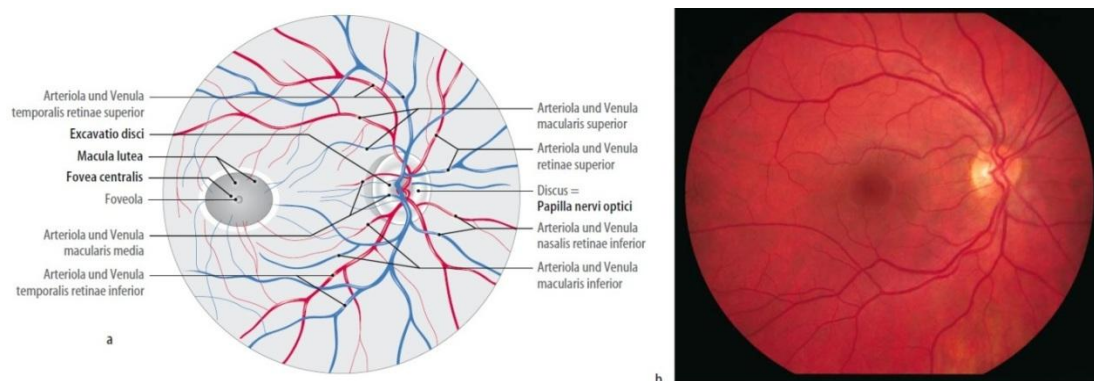

Figure 2.5: **a** – *The blood vessels of the retina of the right eye;* **b** – *Wide angle fundus photograph(from [13])*

On Fig. 2.5 (a) such significant areas of the retina as macula, fovea, foveola and the optic disc are denoted. Those structures are subjects of the research carried out in this project and therefore the more in-detail overview is given here.

The optic disc (approximately 1.5 mm in diameter) (optic nerve head) is the area where the fibers of the optic nerve and the blood vessels of the retina are entering the retina.

Macula is a yellow spot located in the central part of the retina with a diameter of approximately 5.5 mm (15°of the visual field). It contains the fovea, foveola as well as para- and perifoveal ring (which surround the fovea). Since macula is yellow it works as a natural sunblock, adsorbing the excess of blue and UV light.

The fovea, having the highest concentration of the cones, is an area of high acuity of vision with typical diameter of 1.85mm and thickness of 250µm.

Foveola is a region in the center of fovea with the highest visual acuity, where the retina becomes thin. Foveola is avascular, so there is no shadowing on the cone photoreceptors. The typical dimensions are approximately 350µm in diameter (around 1° of visual field) and 130µm of thickness in the thinnest part.

The density of cones is decreasing significantly towards the periphery of the retina, but there are many rods there.
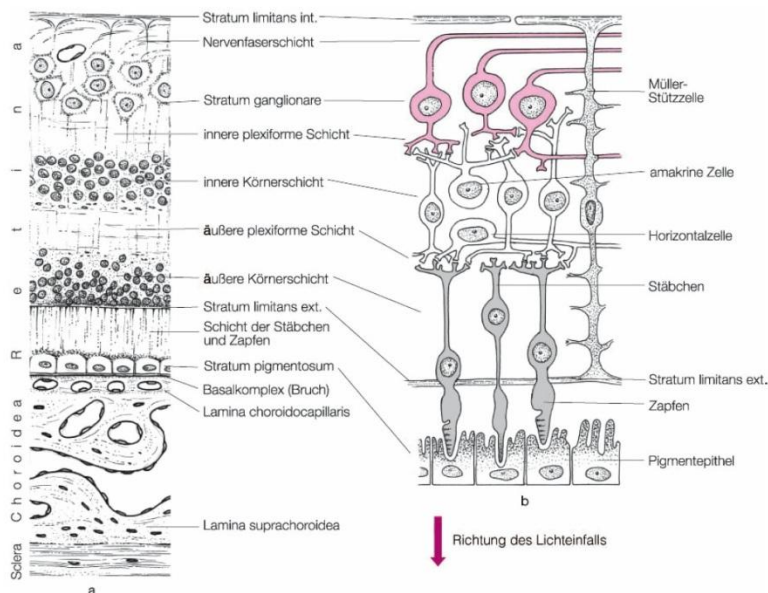

Figure 2.6: *Layers of the retina, choroid and sclera. See text for more information. (from [14])*

The layers of the retina can be observed on the Fig. 2.6. The thickness and the presence of these layers vary depending on the area of the retina, i.e. at the foveola only 6 of them are present.

Top to bottom they are:

Internal limiting membrane (ILM) – a boundary between the retina and the vitreous.

Nerve fiber layer or retinal nerve fiber layer (RNFL) – in human contains the axons of the ganglion cells (see Fig. 2.6 rhs) a capillary network, glial cells and fibers. The thickness of the RNFL in humans varies is location dependent and varies from 10 µm to 400 µm. RNFL has the most polarizing effect on the incident light around the optic nerve head. [15]

Ganglion cell layer (GCL) - contains ganglion cells (see Fig. 2.6 rhs), with a diameter of 10 - 30 µm and a large nucleus. The GCL contains a capillary network of a diameter 10 to 25 µm.

Inner plexiform layer (IPL) - a junction between the ganglion cells of the GCL and the bipolar cells of the INL.

Inner nuclear layer (INL) - consists of multiple rows of nuclei of horizontal cells, bipolar cells, interplexiform cells, amacrine cells and Müller cells (see Fig. 2.6 rhs) as well as dense capillary network, containing capillaries, with a diameter of 5-10 µm.

Outer plexiform layer (OPL) - consists of oblique fibers: Henle's fibers (the axons of the rods and cones) and the dendrites of the bipolar and horizontal cells.

Outer nuclear layer (ONL) - contains rod and cone granules connecting the respective photoreceptors to the OPL.

External limiting membrane (ELM) - selective barrier for nutrients.

Photoreceptor layer (PR) consisting of rod cells and cone cells.

Retinal pigment epithelium (RPE) is responsible for photoreceptor renewal and recycling of vitamin A and absorption of scattered light by its melanin granules. This tissue is able to change the polarization state of the light by polarization scrambling. [16]

The choroid, which is not a part of the retina consists mainly of blood vessels of different sizes (divided to outer layer with larger ones, middle layer with medium size ones and inner layer with a capillary network) with very intense blood flow and its function is oxygen and nourishment delivery to the outer part of the retina. The choroid supplies about 65-85% of the total retinal perfusion. [17]

The sclera (the white of the eye) is a protective layer consisting out of collagen and fiber.

2.2.3 Related diseases

There is a variety of diseases, related to the malfunctions in the retinal perfusion, such as branch retinal vein occlusions, clinically significant macular edema (CSME), teleangiectasia, diabetic retinopathy and age related macular degeneration (AMD).

All those diseases are diagnosed with the help of OCT.

Tin ophthalmology PSOCT can help for diagnosis of keratoconus, glaucoma and AMD. [16]

In this work we focus on the retinal measurements, in which the main applications of PS OCT are diagnosis of AMD and glaucoma. Therefore keratoconus (a degenerative disease of the cornea) is not discussed in this work.

AMD is a disease of the retina in which the macula is getting detached from the choroid, which is the most common reason of visual impairment in older adults. Under the condition of AMD the central vision is damaged whereas the peripheral vision remains unaffected. The mechanism of AMD can be either of following: the drusen (cellular debries) accumulate between the RPE and choroid or the overgrowth of vessels from the choroid directed outside of the corresponding layer to the retina can cause the detachment of the retina. [19]
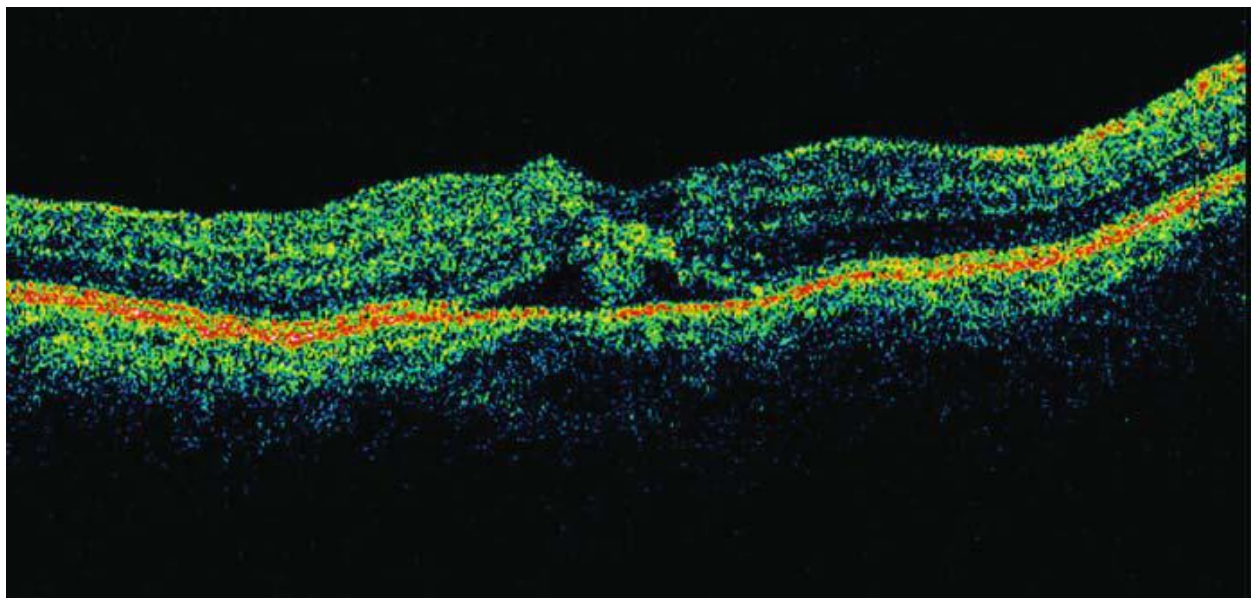

Figure 2.7: *Serious Retinal Detachment (from [19])*

Fig. 2.7 shows retinal detachment, in this case anterior to the RPE band and external to the photoreceptor outer segments. Similar picture can be observed at patients with AMD

Figure 2.8: *Advanced AMD with clear disciform scar observed in the middle. (from [19])*

Fig. 2.8 shows the AMD condition when a scar tissue was formed and large macular venules penetrate the scar to communicate with choroidal circulation.

Glaucoma is an eye disease in which the growth of intraocular pressure may lead to the damage of the optic nerve and thus cause a significant decrease of vision. It is a worldwide leading cause of blindness and therefore it is necessary to diagnose this disease on early stages.[20] The disease is associated with progressive degeneration of the retinal ganglion cells, axons, soma and dendrites. It is reported that the combination of RNFL measures as well as the ones acquired from the optic nerve enables the differentiation between healthy eyes and eyes with early and moderate glaucomatous damage which precedes glaucomatous visual field loss. [19,21]

It is reported that in 60% of the cases the detection of visual field defects is preceded by RNFL defects by approximately 6 years. Detection and registration of the RNFL in the area of macula is very important, since about half of all the retinal ganglion cells lie in the macular region, which enables one to detect an early cell loss.

The posterior segment OCT allows registration of the RNFL the thickness of which is later evaluated by the medical doctors.

For instance, RNFL thickness charts, comparing the patient's data to the normative data display used for OCT guided progression analysis (see Fig. 2.9 and 2.10) and thickness maps methods (see Fig. 2.11) with corresponding software were developed to help the medical facility to interpret the information obtained from the OCT scans. [22, 23, 24]
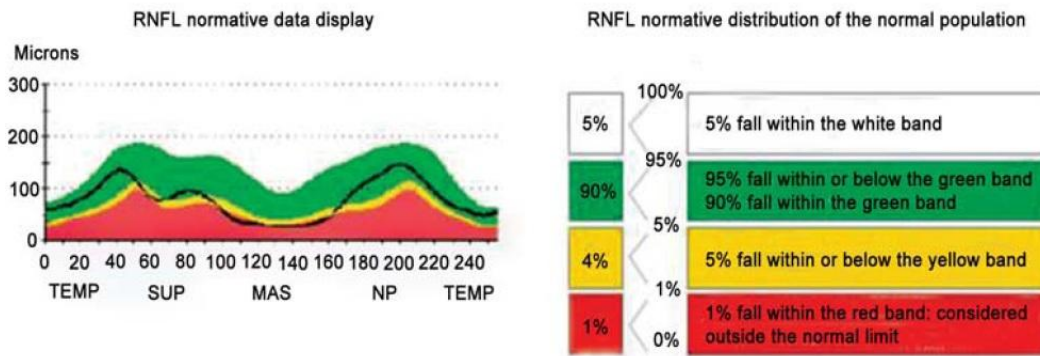

Figure 2.9: *Statistical significance and normative database of the RNFL thickness. (from [22])*
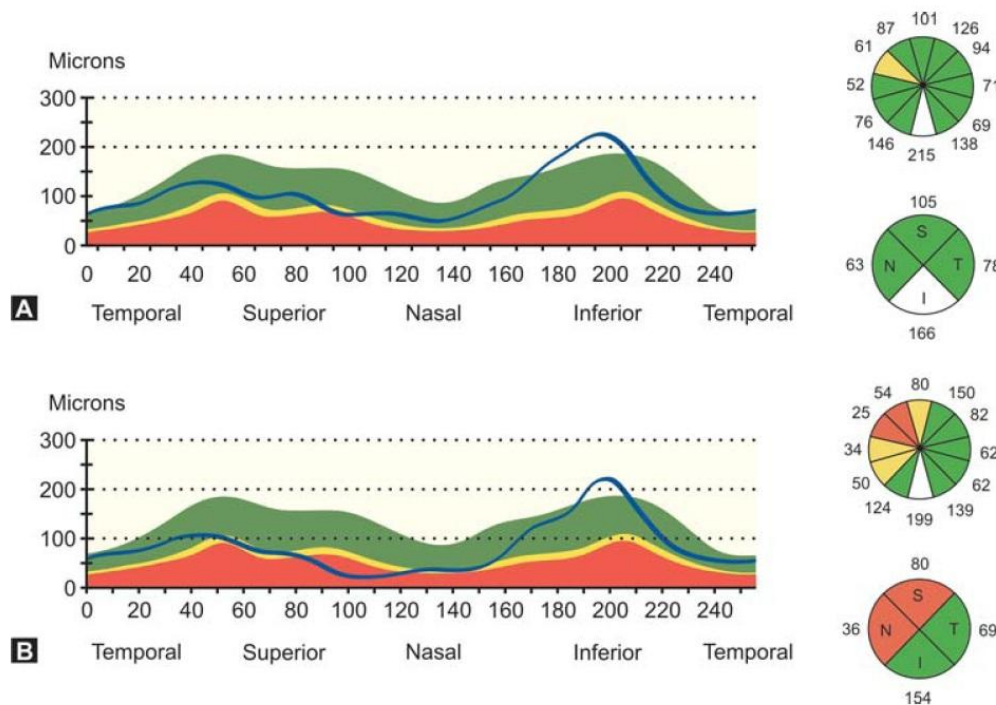

Figure 2.10: *The blue line on the normative data displays (lhs) denotes the patient's results, the sectorial charts on the rhs (from [23])*
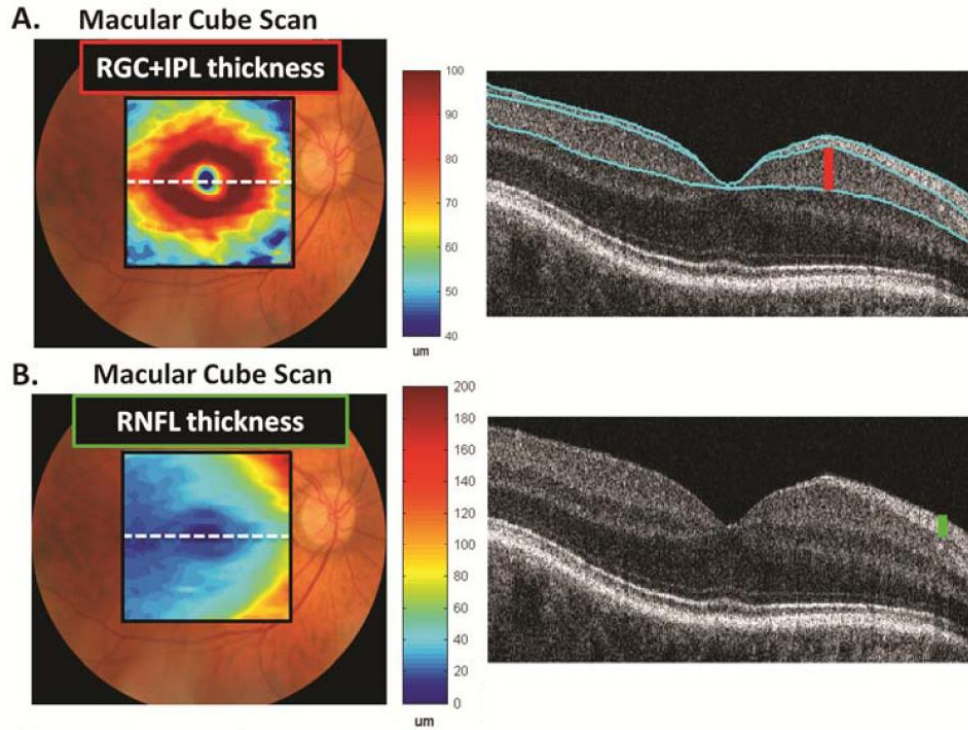
Figure 2.11: *Sample thickness maps and scans from a healthy subject (from [24])*

Clinical studies suggest that direct detection of changes in the ganglion cell layer and RNFL can help for early diagnosis. Since the resolution of the nowadays Spectral Domain Tomography reaches 2-5µm there is a belief that ganglion cell bodies themselves (which diameter varies between 10 to 30 µm) could be detected and studied. However, the contrast in the RNFL, where unmyelinated axons of retinal ganglion cells are located achieved so far by different working groups is not sufficient for that. The reflectance of RNFL is proportional to its thickness. However, the reflectance is directional (due to structural cylindrical elements of the RNFL) hence equally thick areas that are located in different regions may appear not equally bright, dependent on the geometry of observation. Polarization properties of the RNFL are related to its ultrastructure, thus the early structural change can be detected. [15] Therefore the motivation of further investigations on high resolution PS OCT is that with help of additional contrast information available from the polarization pattern on the retina obtained by means of the PS OCT the ganglion cells just below the RNFL can be better contrasted.

3 Polarization Sensitive Optical Coherence Tomography

3.1 Method description

One of the realizations of the PSOCT systems is briefly described in Chapter 2. In this work another system which is based on the same principle was used that needs only a single spectrometer and overcomes therefore system complexity and costs of using two spectrometers. Two reference arms with orthogonal polarization states are used and with an electro-optic modulator (EOM) in one of them. The modulations introduced by the EOM affect only the phase of the polarization component which is parallel to the fast axis, whereas the orthogonal component remains unmodulated. Introducing a modulation by the EOM that appears across a B-scan, i.e. along the lateral scanning coordinate, the separation of the spatial spectra of both polarization components can be achieved: the spatial spectra of the modulated part appears shifted from the zero position. The signal from the two orthogonal polarization components is then divided in the spatial frequency domain into two separate channels by simple band pass filtering. This allows analyzing the polarization properties of the sample in depth with just one spectrometer based on a fast CMOS sensor. [4]

The four-step modulation function (driving the EOM) was designed and used, introducing incremental phase-shifts of π/2 between adjacent A-scans to the vertically polarized component. (Fig. 3.1)
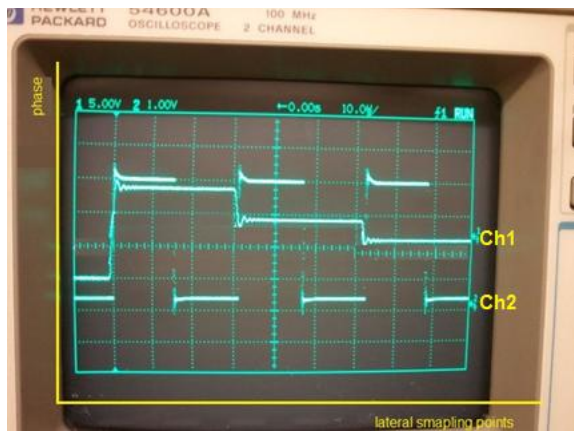

Figure 3.1: *The output of function generators: Channel 1: Four-step modulation function driving the EOM (phase steps: π/2, π and 3π/2). Channel 2: Camera trigger.*

The system acquires full spectral B-scans in k space.

In the postprocessing firstly the Fourier transform along the B-scan direction (x-direction) is performed (Fig. 3.2 (a)) to obtain the spatial frequency spectrum for each wavenumber k.. Thus the two polarization components appear separated (Fig. 3.2 (b)). In the next step the two orthogonal polarization components are extracted by low and bandpass filtering from the spatial frequency spectrum (Figs. 3.2 (c), 3.2 (d), 3.2 (e)). The signals from each polarization states are then handled separately and are inversely Fourier transformed back to k domain. In the final step the two signals are finally Fourier transformed with respect to k, giving the complex valued tomograms ($I_{\parallel}(z)$ and $I_{\perp}(z)$), allowing extraction of amplitude and phase information for each polarization component (Figs. 3.2 (f) and 3.2 (g)).

Retardation $\delta(z)$ is then calculated according to the equation (2.3): $\delta(z)= atan(|I_{\parallel}(z)|/|I_{\perp}(z)|)$.
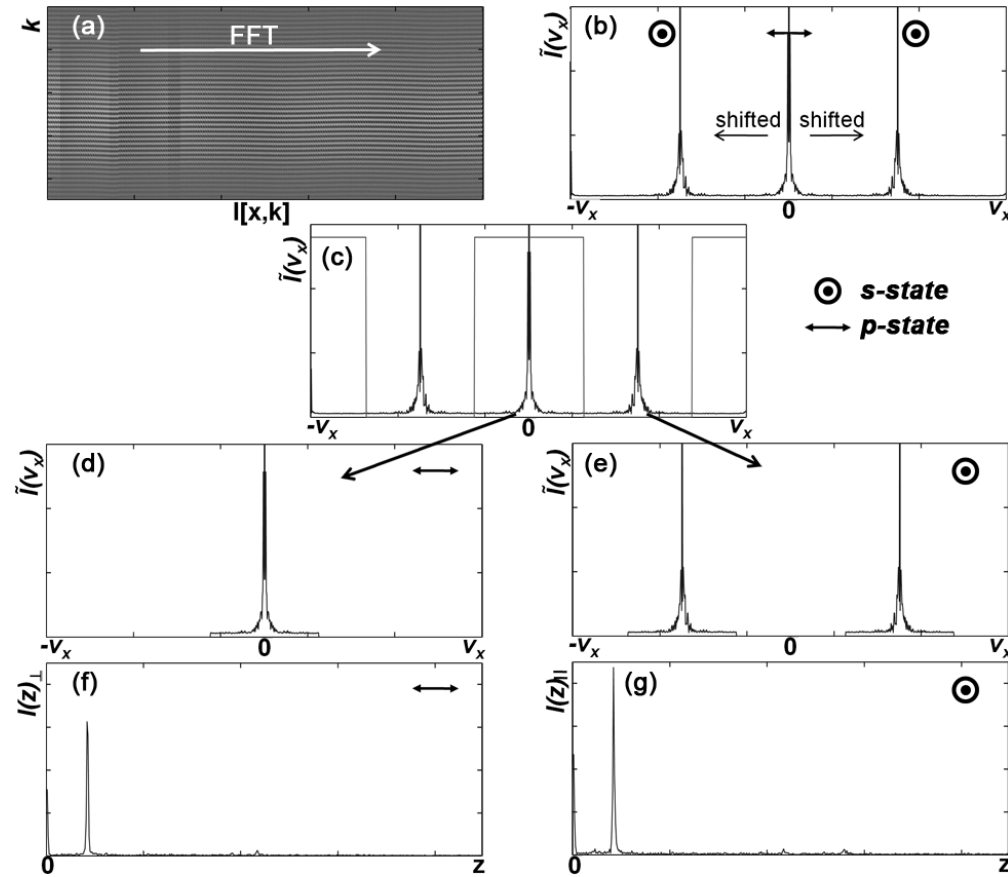

Figure 3.2: *Polarization separation scheme. See text for details.*

The proportions of the lateral structure's spatial-frequency spectrum are one of the sources of the errors in this method. This topic will be handled more in detail in the section "3.6: Aspects of oversampling factor". (from [4])

3.2 Experimental Setup

The ophthalmic Spectral Domain Optical Coherence Tomography (SDOCT) setup allowed parallel acquisition of orthogonally polarized spectra with a single camera and an electro-optic modulator (EOM). The scheme of this setup is presented in Figure 3.3.

A superluminescence diode (Exalos, Inc.) at 830nm center wavelength and 45nm FWHM bandwidth was used as a light source. The power registered in front of the sample was 400-550µW, which is still below laser safety standards. The light beam coming out of the light source is transmitted via an optic fiber the second end of which is fixed at a collimator (FC).

Before the light reaches the first beam splitter of the interferometer which directs half of the light intensity into the sample arm (SA), the light is linearly polarized at 0 degree, which matches the fast axis of the electro-optic modulator (EOM). [1]

The SA:

The sample arm holds a quarter wave plate (QWP) oriented at 45 degree, designed to change the polarization state of the light illuminating the sample into circularly polarized. The beam is then directed to the scanners (an X-Y- galvo scanner unit (SC)). There are two telescopes rescaling the incident beam diameter: the one with a magnification power of 2 installed on the SA beam way after the scanners and before the sample (L-L) as well as an additional telescope with magnification power of 2,5 installed between the dispersion compensation element and the beam splitter in a sample arm.

The Reference Arms (RAs): The light in the common reference arm is split by a beam splitter, into two reference arms. The relative path length, between the two reference arms, is adjusted by a translation stage place in one of them. The common part of two reference arms holds components for dispersion compensation (DISP) between the reference arms and the sample arm. The necessity of matching the dispersion comes from the fact that there are two telescopes used in the SA, one of which is even passed by the light twice, meaning that the light

from the SA is passing all in all 6 lenses and twice a QWP before it reaches the detector of the camera; whereas in the RAs only two beam splitters and 2 polarizing plates introduce dispersion. The light beam travelling in the reference arm, containing the EOM stays linearly polarized at 0 degrees (vertically). It becomes modulated by the EOM. There is an additional couple of polarizers used in this RA: one to ensure the proper polarization state after multiple reflections, the other one to compensate for dispersion difference introduced by a polarizer in another RA), while the polarization state of the light in the other RA is firstly polarized at 0 degrees as well (to ensure the proper polarization state after multiple reflections) and then rotated 90 degrees by a half-wave plate (HWP) oriented at 45 deg. Moreover, the crystal (LiNbO$_3$) of the EOM introduces the dispersion mismatch between the RA with the EOM, the RA without the EOM and the SA. This is connected to the dependency of refractive indexes of the LiNbO$_3$ crystal in the EOM on the polarization state of the travelling through it light. Therefore, the relative dispersion between the two orthogonal polarization states is compensated by placing an additional LiNbO$_3$ crystal of equal length but rotated by 90deg with respect to the fast axis of the EOM into both the other RA and the SA. Both beams from the reference arms are then recombined by a beam splitter.
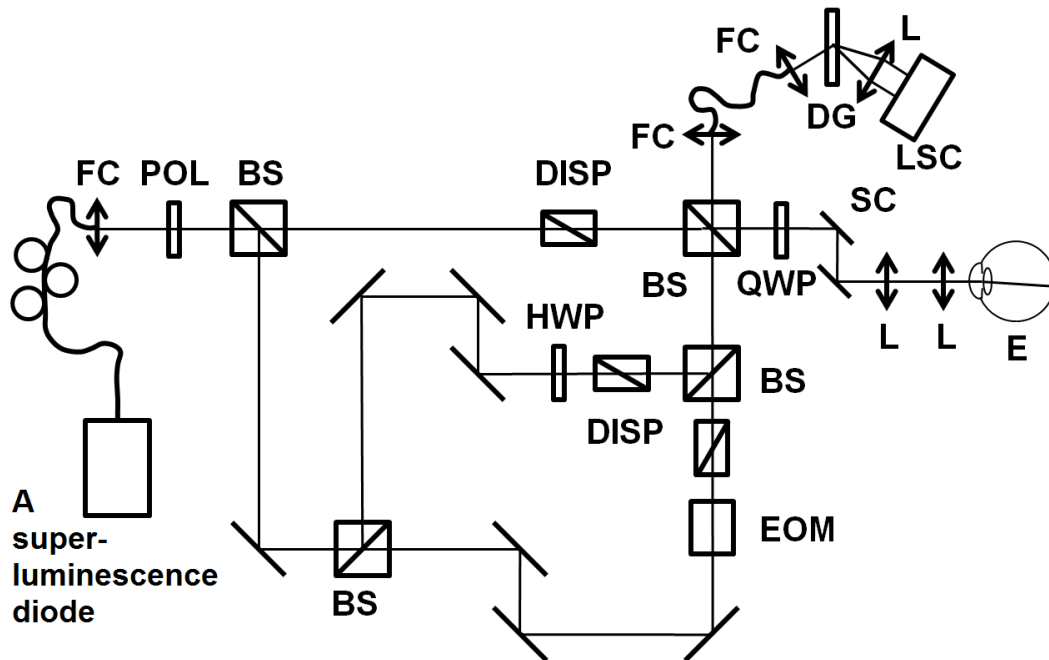

Figure 3.3: *Optical Setup. FC- fiber coupler, POL –polarizer , BS- beam splitter; DISP, dispersion-compensating prism pairs; QWP- quarterwave plate; HWP- halfwave plate; E –eye; SC-scanning unit; L-lens, L-L telescope; EOM - electro-optical modulator; DG - diffraction grating; LSC, line scan camera [4]*

The last beam splitter recombines the light coming from the sample and both reference arms. The light then travels through a single mode fiber towards the spectrometer, which permits line rates of up to 200 kHz. The spectrometer contains a high-speed CMOS detector with 4096 pixels and 12-bit resolution. The light is spectrally dispersed via a diffraction grating (1200 lines/mm) and is collected at a detector by means of an objective (105 mm focal length). 1024 active detector pixels are used to image the full spectrum.

For *in vivo* measurements a mirror reflecting a fixation target was positioned next to the sample arm in front of the patient's second eye unemployed in the measurement in order to minimize eye motion.

3.3 Alignment and modification of the setup for the high-resolution PSOCT

In order to reach the highest sensitivity of the system and the best performance it is crucial to align both RAs and SA as precisely as possible.

The beams emerging from both RAs into the common part of RAs have to be overlapped very precisely and their spectra have to be of the same shape and magnitude (being slightly less than half of the detector saturation value). It is of great importance to make sure, that there is no path difference between the two RAs. This is adjusted via a translation stage for fine alignments in one of the RAs.

The light back reflected or backscattered from the sample is typically of much lower intensity then the one coming from the RAs. It is of great importance to ensure proper coupling into the detector's fiber coupler. For that the series of alignment with a camera able to acquire NIR light were performed.

The necessity of dispersion compensation between the SA containing 2 telescopes introducing effectively 6 extra lenses for the passing light was described in the section 3.2 of Chapter 3. The compensation is performed by two BK7 glass wedges that allow for varying the thickness. The appropriate thickness is derived experimentally by constantly observing the shape and the magnitude of the interference peak during adjustment of the wedges (from a single plain mirror as a sample). In case of the correct alignment the peak should be identical on both sides of the zero belay between the Sa and the RAs.

For *in vivo* measurements of the human retina a transparent chamber containing distilled water50 mm length is placed into the common RA in order to compensate for the dispersion imbalance introduced by the vitreous liquid in the eye.

The spectral density function is measured as a function of the wavelength $S(\lambda)$ by the spectrometer. As a result of the grating based spectrometer the spectrum is measured as hyperbolic function of wavelength. According to equation 2.1 the phase is a linear function in k. Hence the measured spectral interference pattern needs to be mapped to *k* prior to the Fourier transform. A mapping function (a polynomial of the 4th order) was generated empirically once the dispersion was matched in order to rescale the obtained spectrum and the corresponding mapping file was issued. Empiric determination is implemented in following way: while for instance optimizing the shape and magnitude of the interference peak from the SA and RAs the optimal polynomial coefficients can be found. (Fig. 3.4)
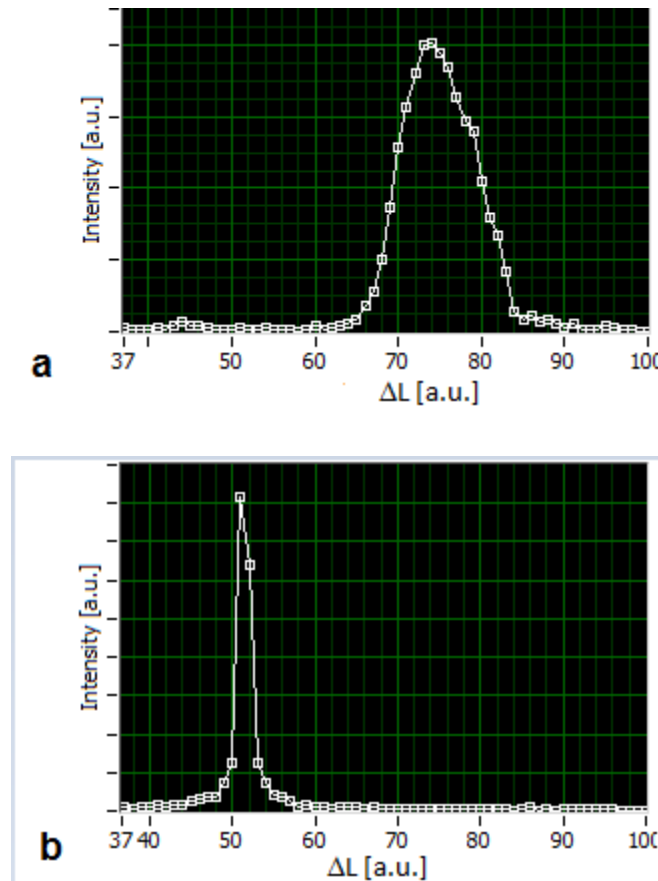

Figure 3.4: *The FFT of the spectral interference pattern* **a** *- before mapping,* **b** *– after mapping*

The EOM is triggered by a function generator with the frequency of f/4, where f is frequency of the camera of the spectrometer. It is important to avoid any phase offset between those two signals by correcting the relative phase via function generator (see Fig. 3.5).
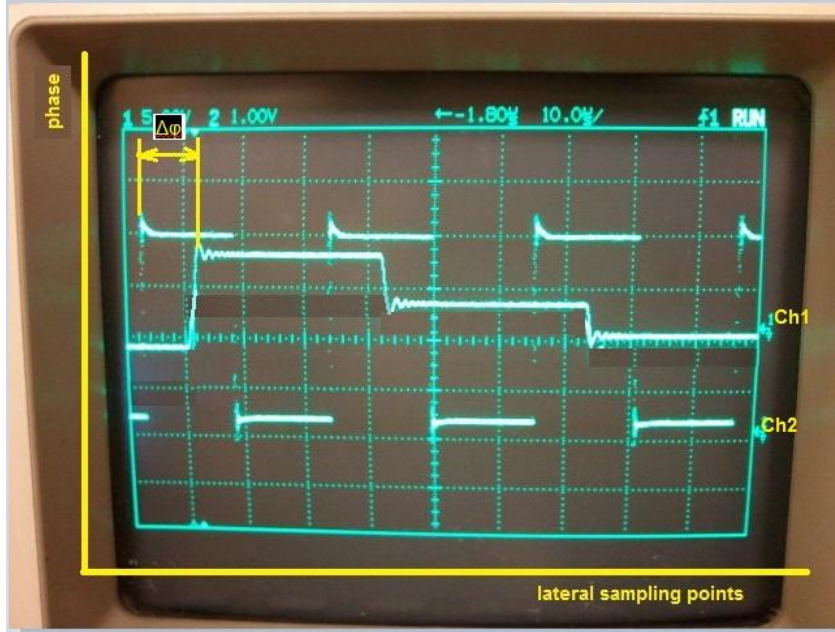

Figure 3.5: *The output of function generators when the phase offset Δφ is present: Channel 1: Four-step modulation function driving the EOM (phase steps: π/2, π and 3π/2). Channel 2: Camera trigger.*

In order to achieve higher resolution the telescope located between the scanners and the sample was exchanged with the one with magnification factor 2 (the lenses with focal lengths of 30mm and 60mm). Thus the beam diameter was enlarged and the spot size on the sample as well as the scanning angle was reduced by factor of 2.

3.4 Data Acquisition and Processing

The data was acquired by means of the Labview software saving it as a custom defined ".OCT" format and was later on processed by a Matlab software code developed in a following way:

Firstly the header information is read out, including the number of A-scan per B-scan and B-scan per volume as well as pixel number per spectrum. Afterwards the external mapping file is loaded and rescaling is implemented which is followed by a subtraction of the background

component, that was recorded with blocked sample arm. The fast Fourier transform along the B-scan direction is carried out and the spatial frequency spectrum is filtered in order to separate the information from both channels, which are then inversely Fourier transformed back to k space. The second Fourier transform is performed with respect to k on both channels and intensity and phase information are revealed for both of them. The stacks of reflectivity and retardation images are created and thresholding is carried out in order to enhance the contrast of the obtained results. After that the results are saved.

The registration of the volumes obtained is carried out by a special plugin of ImageJ software.

3.5 Characteristics of the system

The performance of the system is introduced in this section. The sensitivity, depth range, axial and transverse resolution as well as dependency between the scanning angle and the voltage on the scanners are described.

3.5.1 Sensitivity

The sensitivity of the system was determined experimentally by using a mirror as a sample, the reflectivity of which is assumed to be 1. In order to attenuate the signal reflected from the sample a neutral density filter D=1,7 was installed within the sample arm. (Fig. 3.6)
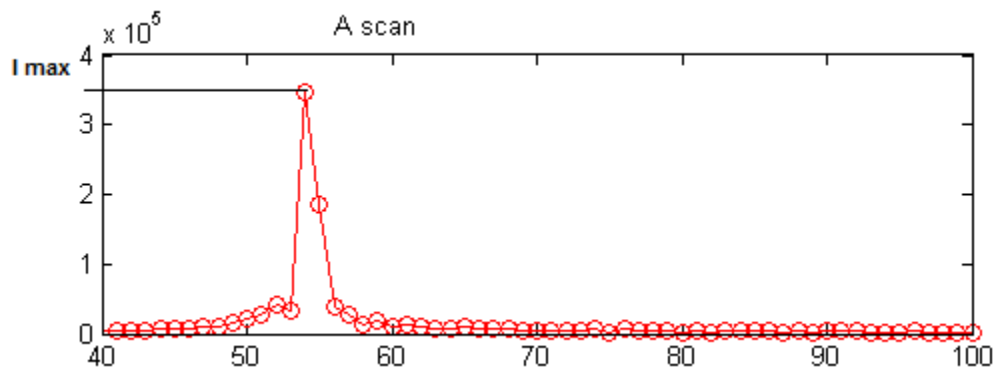

Figure 3.6: *An A-scan depicting the reflection peak from a mirror.*

The power of the signal in a reference arm was attenuated by an additional neutral density filter placed within the reference arm in order for the line scan camera not to come above its saturation limit. The sensitivity then can be measured as follows:

$$\Sigma = 20 \log \left(\frac{I_{max} - M_{noise}}{\sigma_{noise}} \right) + 20D \qquad \qquad (3.1)$$

Where I_{max} is the amplitude of the peak, M_{noise} the mean value of noise and the σ_{noise} is the standard deviation of noise. Thus with a measured peak amplitude of $I_{max} = 3{,}514 * 10^5$, a noise floor of $M_{noise} = 974$ and a noise standard deviation of 597 we obtain:

$$\Sigma = 56 + 34 = 90 dB$$

This sensitivity was measured with a power on the sample of 541µW and a camera frequency or A-scan rate of 32kHz.

3.5.2 Maximum depth range

Depth range in SDOCT is limited by the spectral resolution of the spectrometer.

It can be calculated according to the equation 2.2

The maximum depth range is therefore with N=1024, our central wavelength of 830nm and full spectral range of 45nm:

$$\Delta z_{max} = 3{,}92 mm$$

3.5.3 Light power and beam diameter at the sample

The measured power on the exit of the telescope before the sample is 541µW, which is within the limits prescribed by laser safety.

The beam diameter on the exit of the scanners is. $d_{sc} = 1{,}3\ mm$ (Fig. 3.7) and the one at the exit of the telescope in front of the sample $d = 2{,}8\ mm$. (Fig. 3.8) They were measured with a beam profiler hardware "WinCamD" and software "DataRay" v7.1F both obtained from DataRay.
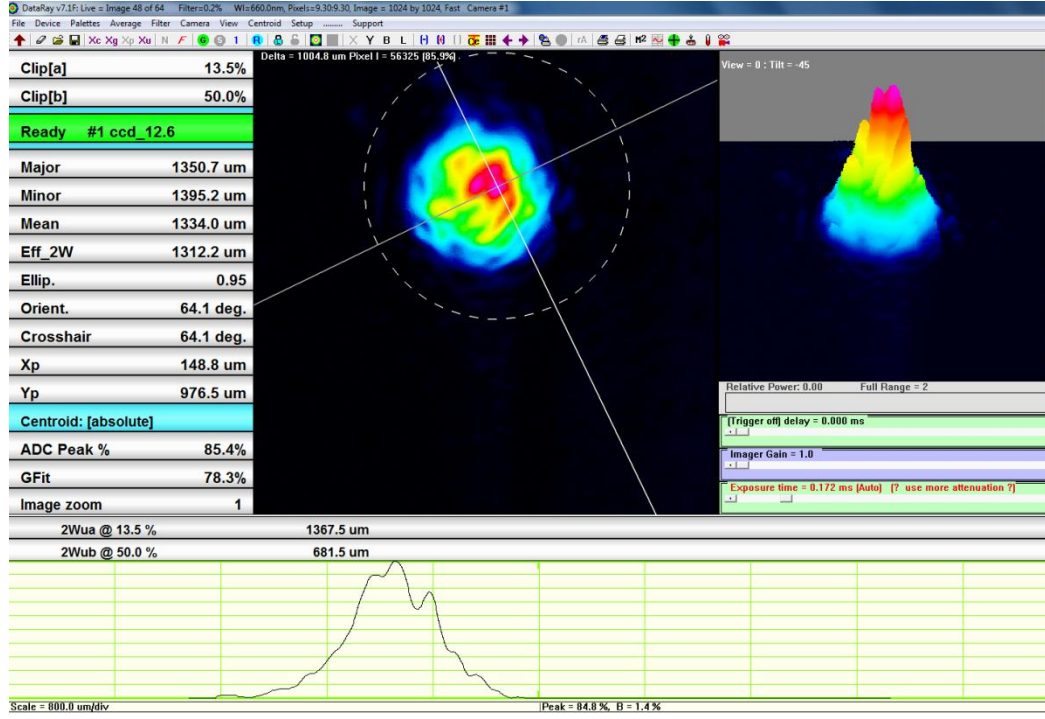
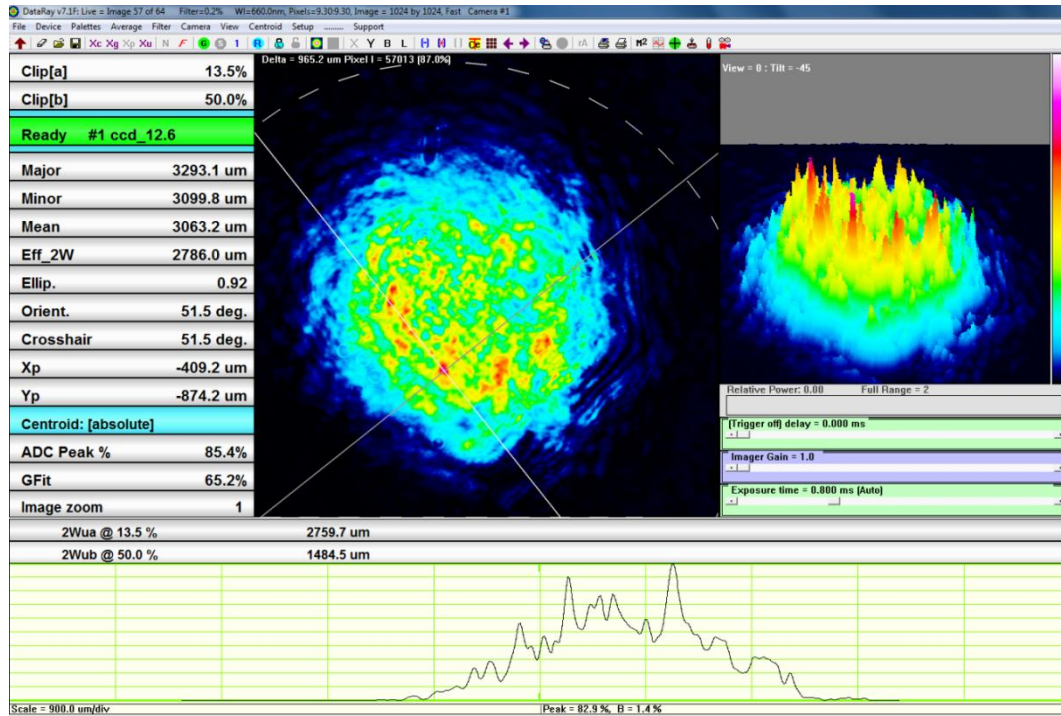**Figure 3.7:** *The beam diameter in the SA measured at the scanners* $d_{sc} = 1,3\ mm$

Figure 3.8: *The beam diameter in the SA measured after the telescope* $d = 2,8\ mm.$

The experimental beam diameter at the sample is close to the theoretical one. Since the magnification factor of the telescope is 2 the beam diameter after the telescope was supposed to be:

$$d = d_{sc}\frac{L2}{L1} = 2{,}6mm$$

Where L1 and L2 are the focal lengths of the lenses used, respectively 30mm and 60mm.

3.5.4. Axial and transverse resolution

As already discussed in Chapter 2 axial and transverse resolution are decoupled in OCT.

The axial resolution is defined by round trip of the light coherence length and is inverse proportional to the bandwidth of the light source and independent of focusing optics. It can be calculated by:

$$\delta z = \frac{l_{c_{FWHM}}}{2} = \frac{2ln2}{\pi}\frac{\lambda_0^2}{\Delta\lambda} \quad . \tag{3.2}$$

With the spectral properties of the employed light source: central wavelength λ_0 of 830nm and full spectral range $\Delta\lambda$ of 45nm, the theoretical axial resolution in air is $\delta z = 6{,}8\ \mu m$

According to the equation 2.6 the spot size can be calculated as follows:

$$\delta x = 2\frac{\lambda_0 2f}{\pi d} \tag{3.3}$$

Where d is the beam diameter at the sample given above. Taking into consideration, that f is the focal length of the focusing optics the spot size for different samples can be calculated. Table 3.1 shows the results of the calculations for the samples used in this work. More detailed information about the samples and the measurements carried out on them is presented in Chapter 4.

Table 3.1

Sample	Focal length of the focusing optics, f [mm]	Spot size, δx [µm]
Tape specimen (stack of paper tape glued together in layers)	30	11,4
Human eye	25	9,5

3.5.5 Scanning angle and voltage on the scanners

The scanning angle α is defined by the voltage applied on the scanners and is α=2β, where β is a mechanical angle by which the scanners are rotated during the measurement. (Fig. 3.9 (lhs))
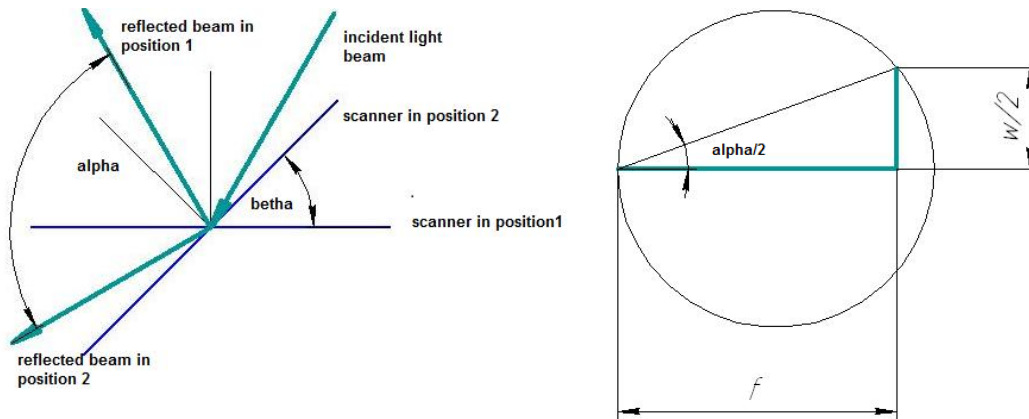

Figure 3.9: (lhs) A schematic representation of the scanners, scanning angle α and mechanical angle β. (rhs) connection between the scanning distance, focal length of the focusing optics and the scanning angle

Transverse scanning range can be defined as following (Fig.3.9 (rhs)):

$$w = 2 * f * tg\frac{\alpha}{2} \qquad\qquad (3.4)$$

where f is the focal length of focusing optics.

Since the telescope with magnifying power 2 was used in the sample arm after the scanners scanning angle is twice less than the one after the scanners

From the experiment:

At the distance of 1 meter for different values of the peak to peak voltage the scanning range was measured. (Table 3.2)

Table 3.2

V_{p-p}, V	w,mm	α, °
0,5	12,5	0,72
1	25	1,43
1,5	40	2,29
2	50	2,86
2,5	65	3,72
3	75	4,30
3,5	90	5,15
4	105	6,01
4,5	115	6,58
5	130	7,44
5,5	145	8,29
6	160	9,15
6,5	172	9,83

The interpolation was performed and the relation between the peak to peak voltage applied to the scanners and the scanning angle was found out:

$$V_{p-p} = 0{,}655\alpha \qquad\qquad (3.5)$$

The scanning angle α (before the magnifying telescope, whereas the scanning angle after the telescope equals the mechanical angle of the scanners β) is calculated according to the equation:

$$\alpha = 2 * arctg\left(\frac{w}{2*f}\right) \qquad\qquad (3.6)$$

3.6 Aspects of oversampling factor

In coherent imaging the width of the detected spatial spectrum (ν_δ) is defined by the inverse transverse spot size δ_x (see equation 3.5) ν_δ =1/ δ_x. When a phase shift of $\Delta\varphi$ between adjacent depth profiles is introduced, the lateral spatial frequency spectrum is be shifted by $\pm\nu_\phi = \pm(\Delta\phi/2\pi)(N/w)$, where N is a tomogram length of depth profiles covering a transverse range w. In this system (see Fig. 3.1) the phase shifts of π/2 are used, which corresponds to half the Nyquist frequency ($\nu_{\pi/2} = N/4w$). The performance of the algorithm depends critically on the ratio between the spatial spectral width ν_δ and the full spectral range N/w. This ratio is called oversampling factor (which is a number of sampling points per spot size). If the oversampling factor is chosen too small, parts of the unshifted spatial spectrum can overlap with the shifted spatial spectrum which would cause crosstalk between the two orthogonal polarization states. In case of cross talk, the calculated polarization values for retardation and axis orientation will be wrong. To avoid such crosstalk it is important in the case of four-step modulation function used in this work, to follow the conditions $\delta x \leq \nu_{\pi/2} = N/4w$. In other words the oversampling factor chosen should be more than 4. [25]

This issue of polarization state separation is crucial for a successful utilization of the method and therefore it was analyzed in various experiments in vitro and in vivo in this work. The results are to be observed in Chapter 4.

4 Measurements and results

In order to support the theoretical calculations of the oversampling factor (see Chapter 3, Section 6) and its influence on the performance of the system a series of practical measurements was carried out both on a special specimen manufactured for these purposes and *in vivo*.

4.1 Measurement on a tape specimen

A specimen consisting of 20 layers of paper tape and a focusing lens with focal length of 30mm was manufactured for the measurements. This sample mimics the human, has the advantage of high reproducibility and the possibility to compare the results for different OCT platforms for retinal imaging.

The speckle size δx for this specimen was calculated in section 3.5.4 and is $\delta x = 11{,}4 \mu m$

A series of measurements carried out on this specimen was designed to illustrate how variation of the oversampling factor influences the performance of the system. The oversampling factor is defined as follows:

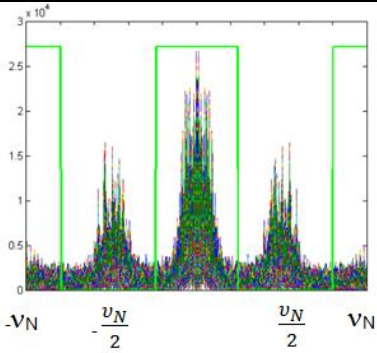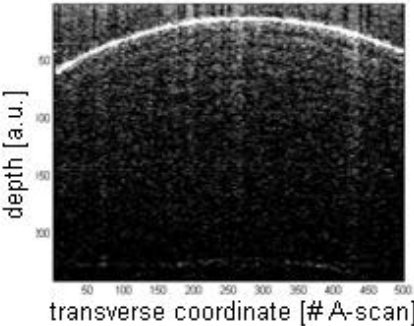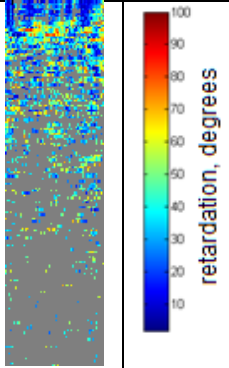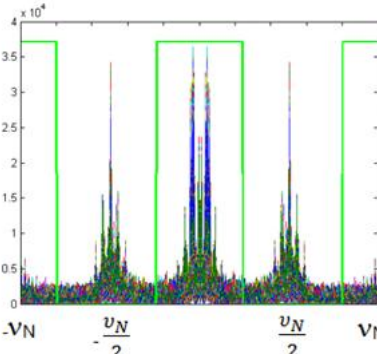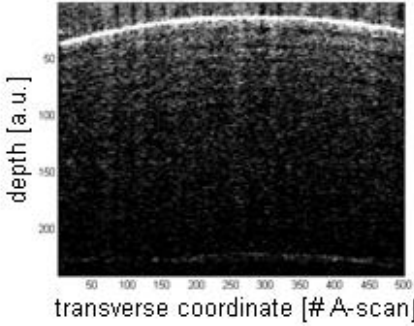$$OSF = \frac{N*\delta_x}{w} \qquad\qquad (4.1)$$

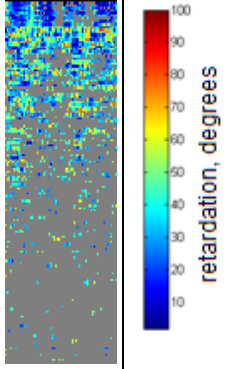5 B-scans were acquired each with a number *N=500* A-scans per B-scan, detector frequency 20kHz and oversampling factors (*OSF*) of 0.7, 1, 2, 5 and 10, respectively. The calculated values of the transverse scanning range (equation 4.1) on the sample *w*, scanning angle on the scanners α (from 3.8) and corresponding peak to peak voltage V_{p-p} (from 3.7), applied to the scanners are presented in the Table 4.1.
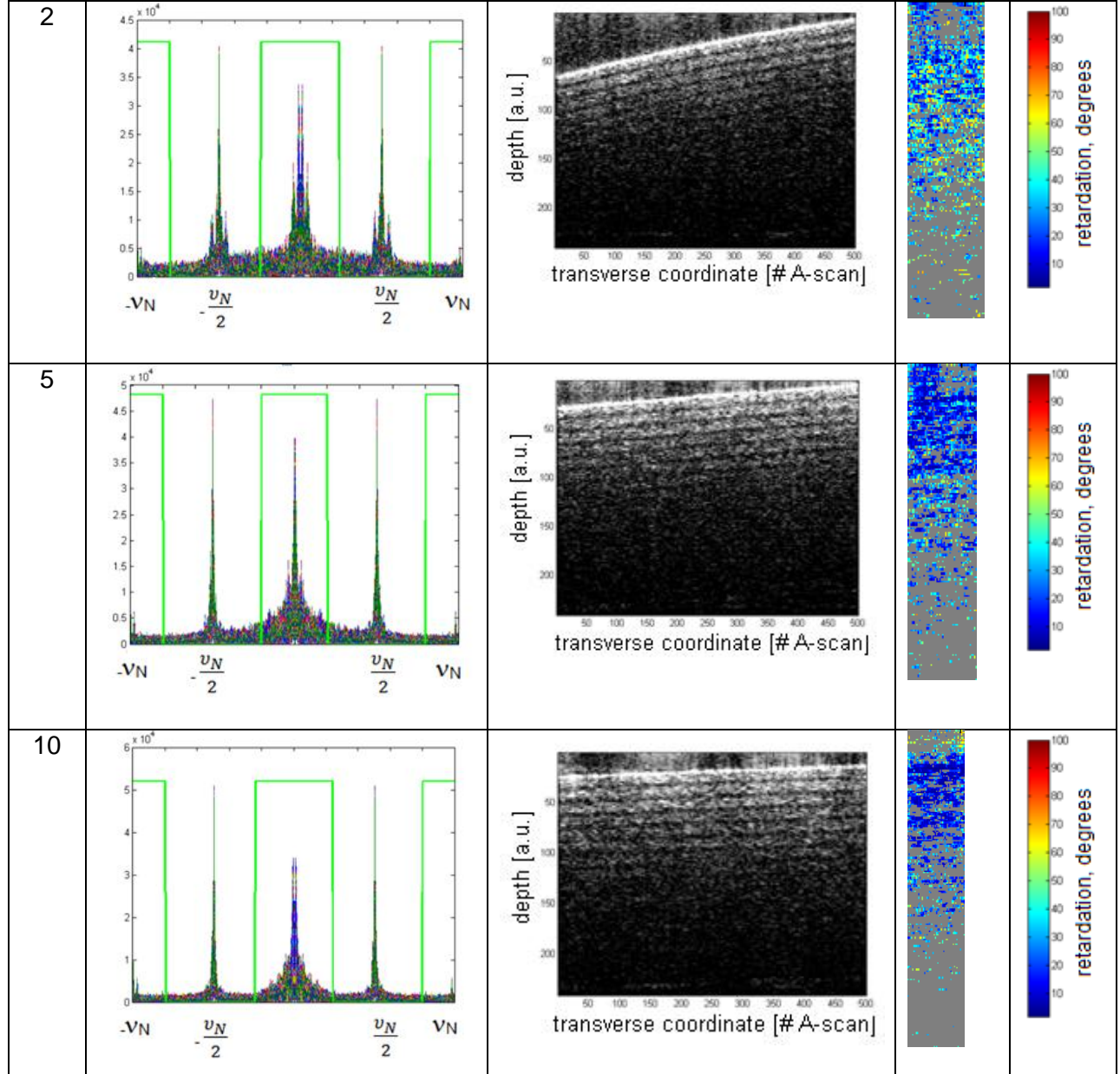
Table 4.1

OSF	w [mm]	α [°]	V_{p-p} [V]
0,7	8,129	15,43	10,10
1	5,690	10,83	7,09
2	2,845	5,43	3,56
5	1,138	2,17	1,42
10	0,569	1,08	0,71

After the post-processing a spatial frequency spectrum, a reflectivity image (calculated from equation 2.3) and a corresponding retardation image (calculated from equation 2.4) were obtained for each of the measurements (Table 2). ν_N in Table 2 denotes the spatial frequency at the Nyquist limit. In the column for the spatial frequencies the result of the FFT for each wavenumber k is plotted in single graph. The DC component discussed in the section 2.1.2 was subtracted in post-processing stage. The green curve in the spatial frequency spectrum represents the band pass filter used for separation of components obtained from two polarization channels.

Table 4.2

OSF	Spatial frequency spectrum	Reflectivity image (B scan)	Retardation image
0,7			
1			

As it can be observed from the Table 4.2 the quality of spectral separation as well as the signal to noise ratio in the OCT tomogram (which is also affected by undersampling) grows with the increasing oversampling factor. The tape itself shows a characteristic layered structure. In order to compare the spatial frequency spectra we plot the spatial frequency spectrum obtained at the center wavenumber k_0 of each OSF in a single figure (Fig.4.1) and put further the resulting retardation images side by side in Fig. 4.2.
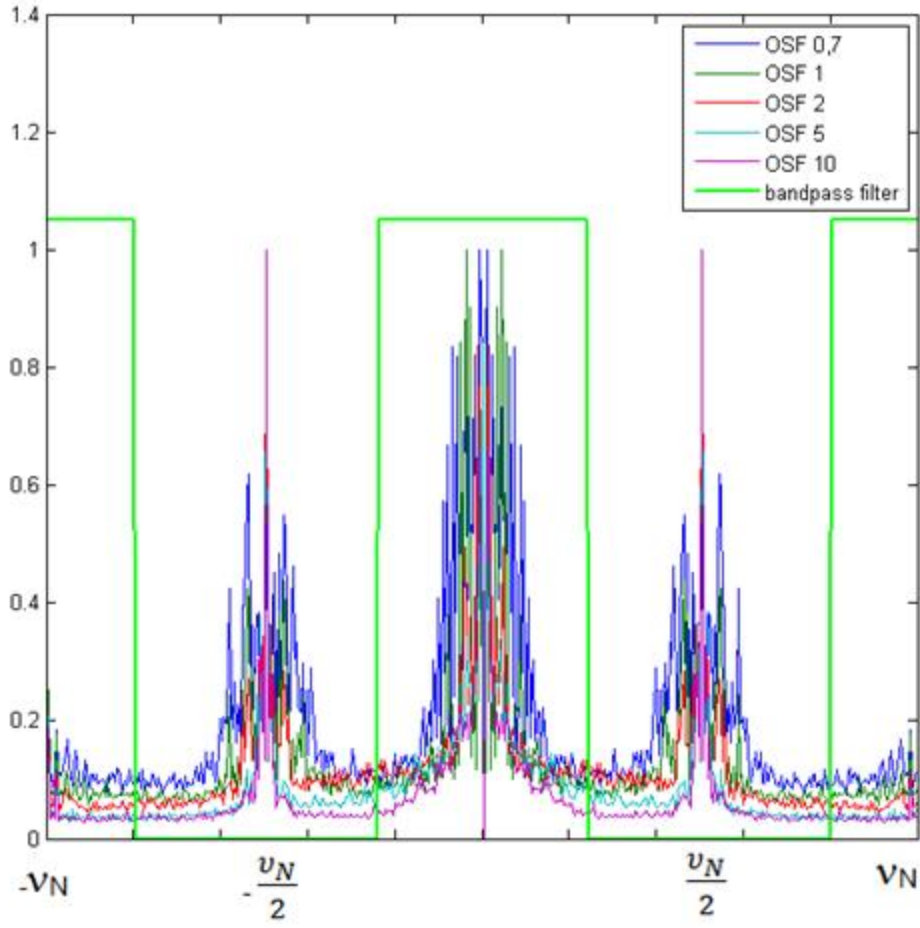
Figure 4.1: *Comparison of the envelopes of the spatial frequency spectrum for one B-scan for oversampling factors 0.7, 1, 2, 5 and 10.*
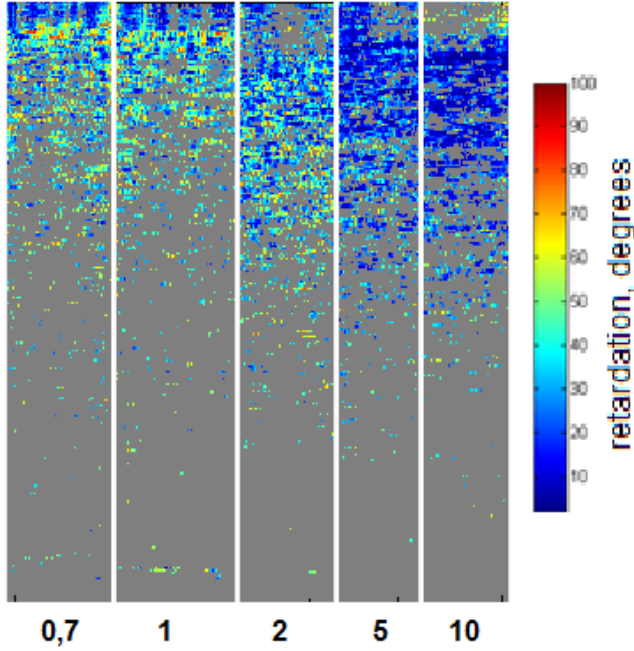
Figure 4.2: *Comparison of the retardation for the oversampling factors 0.7, 1, 2, 5 and 10.*

It is obvious from Fig. 4.1 that with growing OSF the width of the peaks is getting thinner and from the Fig. 4.2 that the separation quality is increasing with the growing OSF. As a result, the retardation value appears random for oversampling factors < 4, and becomes then defined for higher OSF. In latter case $\delta(z) = \arctan\left[\frac{A_2(z)}{A_1(z)}\right] = 0$ degrees, as represented by blue color.

4.2 In vivo measurements

To prove the trends observed in the previous section measurements *in vivo* were carried out on the retina of healthy volunteer with N=500, camera frequency 32kHz for *OSF* 0.7 and *OSF* 5.

The speckle size δx on the retina was calculated in section 3.5.4 and is $\delta x = 9{,}5\mu m$, assuming that the effective focal length of the human eye is 25mm, together with a beam diameter at the cornea of 2,7mm. [1]

The corresponding transverse scanning range w, scanning angle α on the scanners and voltage applied to the scanners calculated according to equations 3.4-3.6 are presented in the Table 4.3

Table 4.3

OSF	w [mm]	α [°]	V_{p-p} [V]
0,7	6,771	15,43	10,10
5	0,948	2,17	1,42

For the measurement with OSF=0.7 the spectral separation pattern, the reflectivity and retardation images are presented on Figures 4.3-4.4
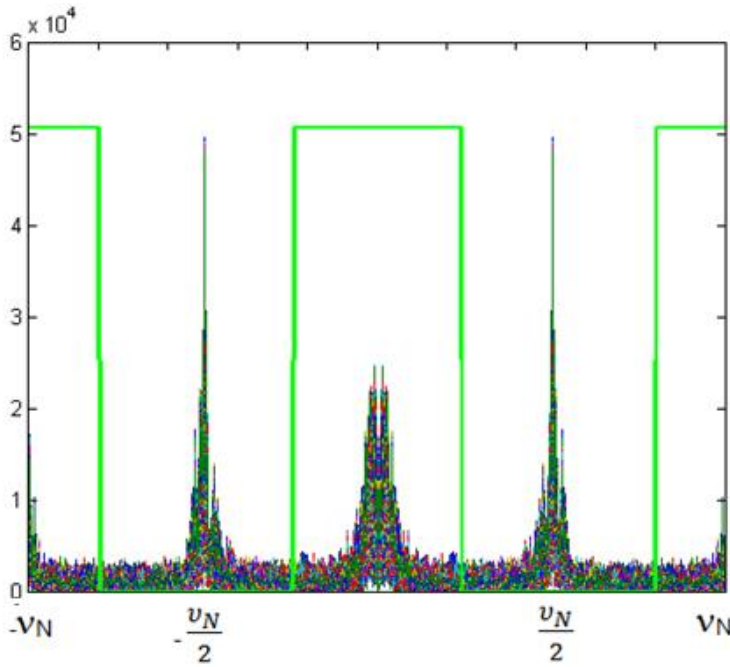

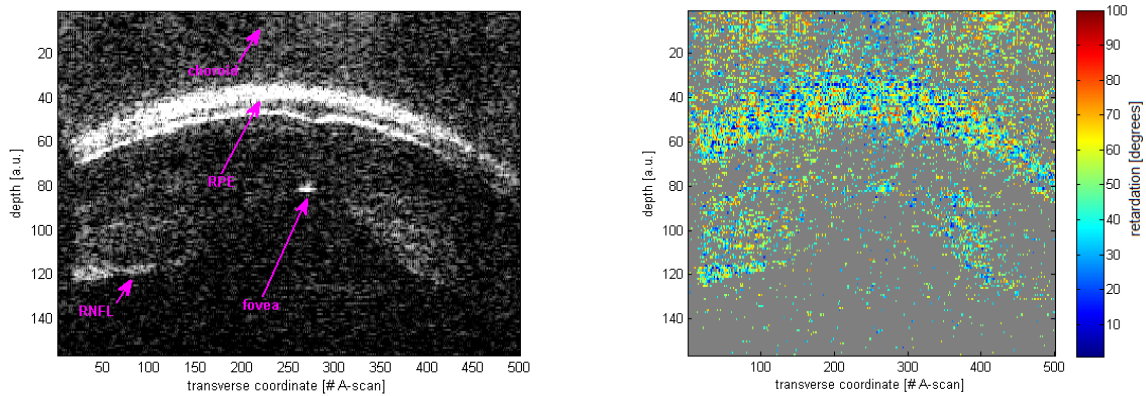**Figure 4.3:** *Spatial frequency spectrum for OSF 0.7*

Figure 4.4: (lhs) *Reflectivity image (B-scan) with denoted fovea, RPE, RNL and choroid and* **(rhs)** *retardation image for OSF 0.7*

From Fig. 4.4 we can conclude that both sensitivity of the system with such low OSF is not sufficient and the spectral separation is not correct. The retardation image shows an irregular pattern without clearly defined retardation value. In theory the retardation should start with zero at the surface (RNFL), would increase during passage of the nerve fiber layer, and stay then constant in the following deeper retinal structures. It increases again in the deeper choroid structures, which are however not visible anymore.

For the measurement with OSF=5 the Spatial frequency spectrum, the reflectivity and retardation images are presented on Figures 4.5-4.6
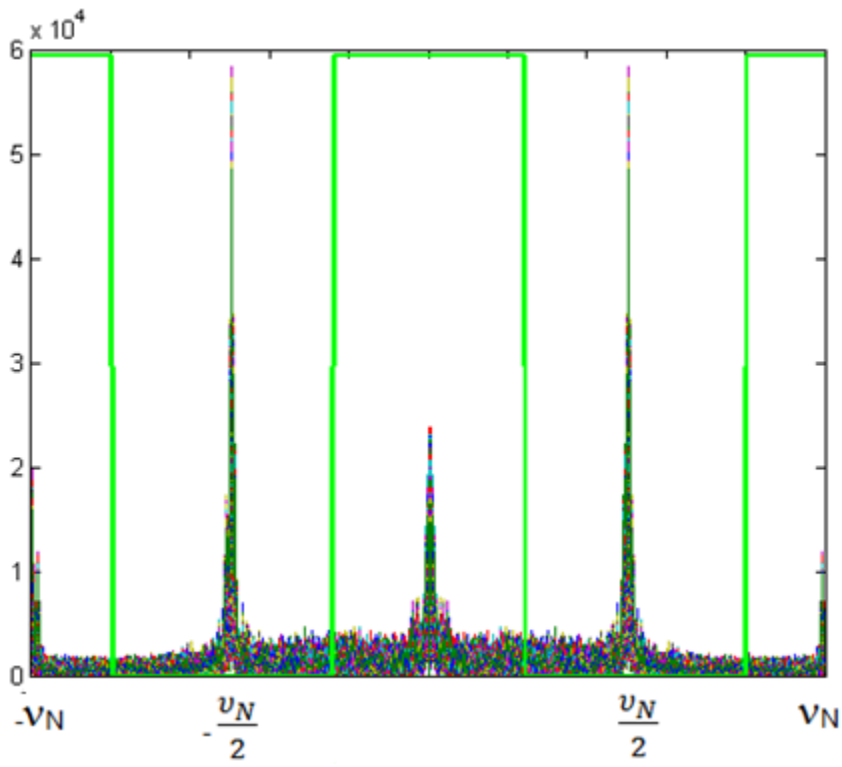

Figure 4.5: *Spatial frequency spectrum for OSF 5*
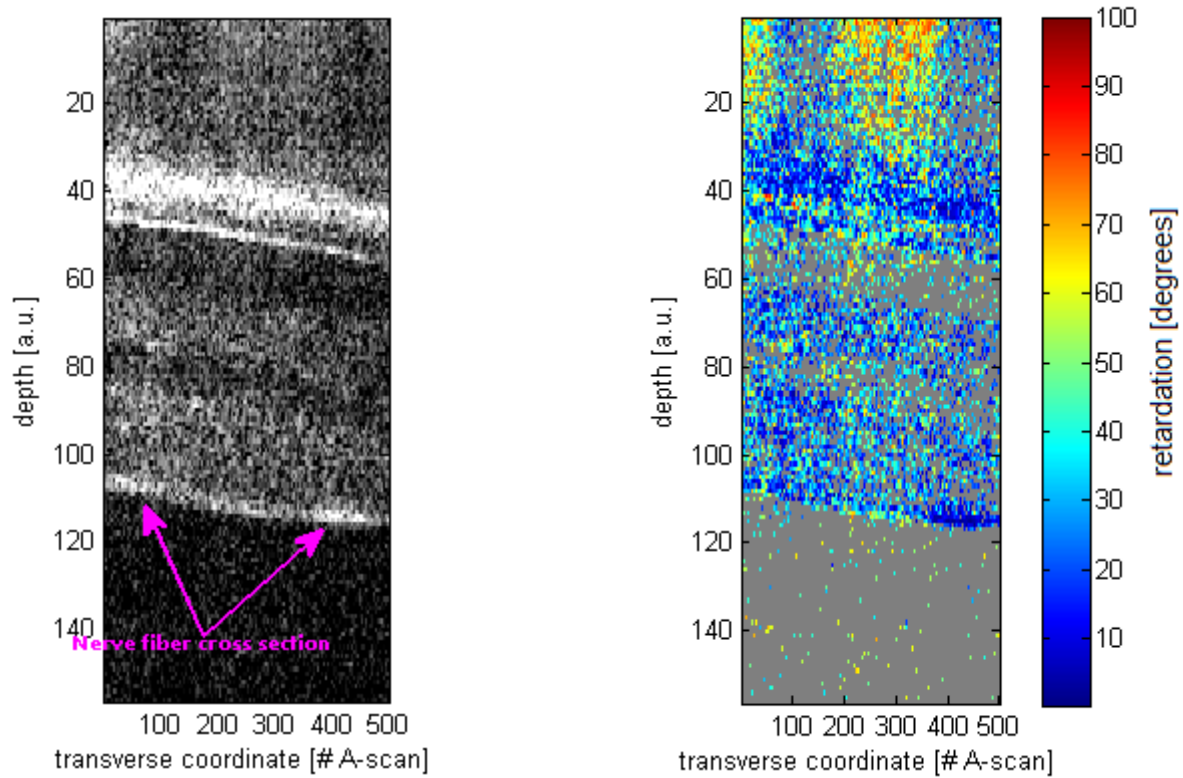
Figure 4.6: (lhs) *Reflectivity image (B-scan) with RNFL marked and* **(rhs)** *retardation image for OSF 5*

From Fig. 4.6 we can again observe, that both the signal to noise ratio and the separation of polarization channels information gets significantly better once the threshold of OSF=4 is overcome. The retardation image could be used to enhance the functional contrast of the reflectivity image in particular for polarization affecting structures such as the retinal nerve fibers. Degradation of those structures will be visible as polarization scrambling, similar to the effect in case of undersampling.

4.3 Discussion

Summarizing the criteria that influence the performance of the system one has to find the optimal combination and best trade off possibility between following parameters:

1. Axial resolution: In order to make full use of the axial resolution that can be achieved in a given setup one has to keep the OSF>2. This expresses the Nyquist limit that for resolving an oscillation a minimal sampling of two is necessary.

2. As calculated from the theory and proven by the measurement results obtained with our PSOCT system with spatial encoding employing a four step phase function, the OSF>4 is sufficient for the successful separation of the information from two orthogonal polarization channels.

3. The field of view / transverse scanning range should be kept as large as possible, since smaller fields of view increase the probability of recognition errors. As an example the B-scan taken with OSF 5 and transverse scanning range of only 0,948mm on Fig. 4.7 can be observed. It is challenging for the eye of the system operator to recognize the region of fovea which can lead to errors. Furthermore, a larger field of view allows for better inspection of retinal structures and the recognition of possible pathologic changes.

4. A curtail for the performance of the system factor is the measurement time. Short measurement times allow keeping motion artifacts during patient measurements small and generally increase patient's comfort. The measurement time is calculated according to the following equation:

$$t = \frac{N_{A|B} * N_{B|v}}{f_d} \qquad\qquad (4.2)$$

Where $N_{A|B}$ is number of A-scans per B-scan, $N_{B|v}$ – number of B-scans per acquired volume and f_d –frequency of the detector (in the case of this work the line rate of a linear array camera).
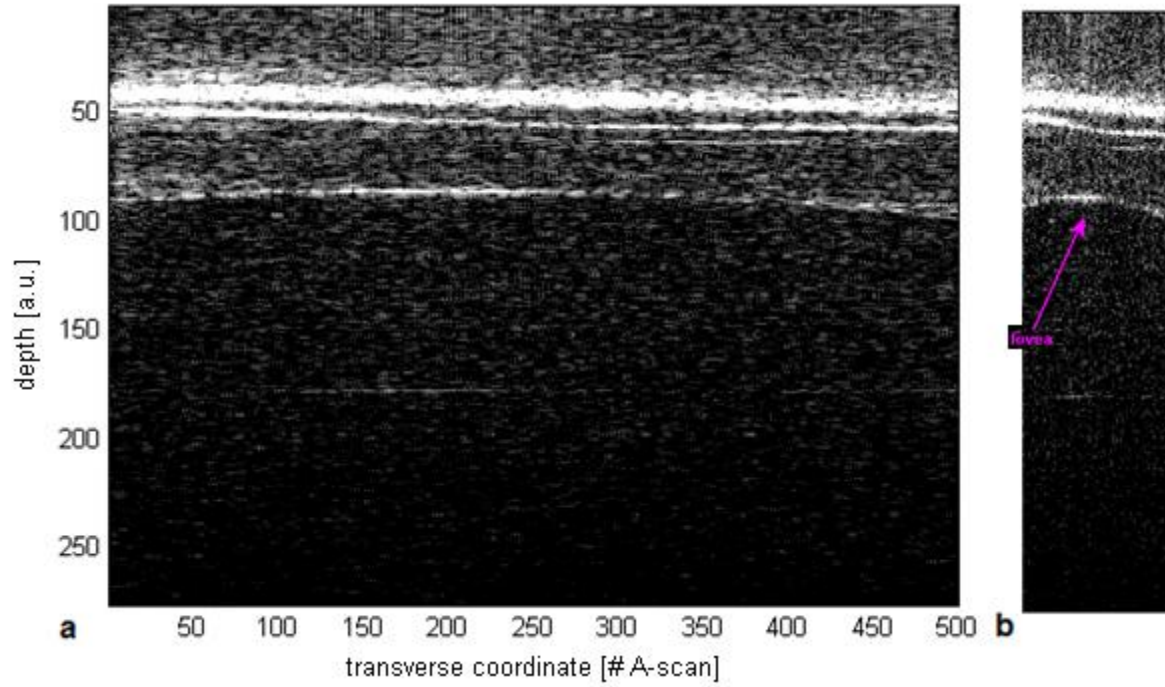
Figure 4.7: a - B-scan of the fovea acquired with transverse scanning range of 0,948mm; b – the same B-scan compressed along transverse direction

Table 4.4 Shows calculated values for OSF and measurement time calculated for the case of 2mm^2 field of view and OSF>4 for the system used in this work for the measurements on human retina ($\delta x = 9,5\mu m$) for the case of rectangular B-scans ($N = N_{A|B} \; N_{B|v} = 500$)

According to equation (4.1)

$N(OSF = 4) = 844$

$N(OSF = 8) = 1685$

Table 4.4

OSF	4	8	4	8	4	8
A-scan rate [kHz]	32	32	64	64	128	128
t [s]	13,2	26,3	6,6	13,5	3,3	6,75

From the Table 4.4 we can observe that OSF and minimum measurement time are inversely related, therefore the compromise between those two parameters has to be found in each particular case. The table also demonstrates how important it is to increase the system speed in order to maintain proper sampling over a reasonably large field of view. The drawback is loss of signal to noise ratio with higher A-scan rates because of lower exposure times. In general it is important to keep the measurement time lower than 10 sec, ideally only a few seconds. In case a retinal tracking system is employed those time constrains are much more relaxed. The fastest reported OCT system for retinal imaging employs the technique of swept source OCT and achieves currently 3.2 MHz A-scan rate with reasonable signal to noise ratio.

5 Conclusion and Perspectives

5.1 Conclusion

In summary the main goal of the work was fulfilled. A single camera high speed PSOCT system based on a novel concept of spatial frequency multiplexing was analyzed. The differentiation between orthogonal polarization channels is obtained through spatial modulation via an electro-optic modulator. This configuration introduces less technical effort and less costs of the whole setup. PSOCT allows for reconstruction both the retardation of the light backscattered from within the sample, as well as the optic fast axis orientation. For simple contrast enhancement the retardation image is sufficient. The system was then redesigned for achieving high transverse resolution for functional retinal imaging employing polarization contrast. In general the transverse resolution is defined by the beam diameter at the cornea. This diameter is ultimately limited by the open diameter of the iris. The system was designed to achieve a lateral resolution of about 9.5 μm on the retina. This resolution is sufficient for resolving small details in the human retina such as individual nerve fiber bundles or small capillaries. The beam at the cornea is 2.7 mm. Beams of larger diameters suffer already from increasing aberrations introduced mainly by the human cornea.

The combination of optimal parameters for the best performance of the PSOCT system with respect to the separation of spatial frequency spectra of both orthogonal polarization states was investigated using a test sample mimicking the human eye that was built for this purpose. The parameters have been verified during *in-vivo* measurements of a healthy volunteer. The discussion about the necessity of keeping the measurement time low in order to minimize motion artifacts and high resolution for which good oversampling is crucial was presented. The highest imaging speed for *in vivo* imaging was limited by the achieved sensitivity. Since both polarization channels are recorded simultaneously with a single camera, the system sensitivity is reduced by -6 dB as compared to a PSOCT system with two spectrometers. The reason is, that first the sample signal is split between both polarization channels and second because only half of the camera saturation level can be used for each signal. An A-scan rate or camera rate of 32 kHz has finally been used for *in-vivo* imaging and allowed for a sensitivity of close to 90 dB.

The presented *in vivo* measurement of the retina demonstrated finally the capability to observe small retinal structures such as individual nerve fiber bundle cross sections, both in the intensity tomogram as well as in the retardation image.

5.2 Perspectives

Clearly the next step is to enhance the functional dimensionality of the imaging space from 3D to 4D, having 3 spatial coordinates and one encoding the polarization contrast. In order to overcome motion distortions during the 3D data recording, sophisticated registration algorithms may be employed [26]. The advantage of such 3D data cubes is that en-face images can be extracted, that usually yield better information about structural integrity, e.g., of full nerve fiber bundles, instead of only cross sections. Also, small microscopic details in the retina such as photoreceptors, or capillary trees are much better appreciated. The hope is also to use the additional contrast for better visualization of details that suffer from otherwise low intensity contrast, as there are ganglion cell bodies or retinal pigment cells. Their non-invasive and label free visualization would have a major impact on the understanding of glaucoma, multiple sclerosis that lead to degeneration nerve fiber tissue, or of age related macula degeneration and other diseases that affect the retinal pigment cells.

The issue of current implementation of the experimental setup being sensitive to vibrations should be solved which would help to achieve better sensitivity and stability as well as better reproducibility of the results. The low frequency modulations distorting and decreasing the quality of the obtained PSOCT data should be studied and eliminated.

The method of spatial frequency multiplexing itself has a perspective of encoding other parameters but polarization state information, such as for instance different depth ranges. One range could cover the full anterior chamber, the second range the retina, which would allow for imaging of the entire ocular structures.

References

[1]   Schmoll, T. (2010) "*Optical Coherence Tomography of Tissue Physiology, unpublished thesis,*" (Phd.), Center of Medical Physics and Biomedical Engineering, Medical University Vienna

[2]   N. Nassif, B. Cense, B. Hyle Park, S. Yun, T. Chen, B. Bouma, G. Tearney, and J. Boer, *"In vivo human retinal imaging by ultrahigh-speed spectral domain optical coherence tomography,"* Opt. Lett. 29, 480-482 (2004).

[3]   Rainer A. Leitgeb ; Tilman Schmoll; *"In vivo functional retinal optical coherence tomography fOCT,"* Proc. SPIE 7163, Ophthalmic Technologies XIX, 71631J (February 23, 2009); doi:10.1117/12.809787.

[4]   T. Schmoll, E. Götzinger, M. Pircher, C. Hitzenberger, and R. Leitgeb, *"Single-camera polarization-sensitive spectral-domain OCT by spatial frequency encoding,"* Opt. Lett. 35, 241-243 (2010).

[5]   B. Hochheimer and H. Kues*, "Retinal polarization effects,"* Appl. Opt. 21, 3811-3818 (1982).

[6]   R. Leitgeb, R. Michaely, T. Lasser, and S. Sekhar, *"Complex ambiguity-free Fourier domain optical coherence tomography through transverse scanning,"* Opt. Lett. 32, 3453-3455 (2007).

[7]   W. Drexler and J.G. Fujumoto (Eds.), *"Optical Coherence Tomorgaphy: Technology and Applications,"* Biological and medical Physics, Biomedical Engineering (2008)

[8]   Fercher AF., *"Optical coherence tomography - development, principles, applications,"* Z Med Phys. 2010;20(4):251-76. Epub (2009)

[9]   E. Gotzinger, M. Pircher, B. Baumann, C. Hirn, C. Vass, and C. K. Hitzenberger, *"Retinal nerve fiber layer birefringence evaluated with polarization sensitive spectral domain OCT and scanning laser polarimetry: a comparison,"* J Biophotonics 1, 129-139 (2008).

[10]   Tilman Schmoll ; Erich Götzinger ; Angelika Unterhuber ; Christoph K. Hitzenberger ; Rainer A. Leitgeb; *"Ultra-high-speed polarization sensitive OCT in the human retina using a single spectrometer,"* Proc. SPIE 7889, Optical Coherence Tomography and Coherence Domain Optical Methods in Biomedicine XV, 78890U (February 11, 2011); doi:10.1117/12.875708.

[11]   Erich Götzinger, Bernhard Baumann, Michael Pircher, and Christoph K. Hitzenberger *"Polarization maintaining fiber based ultra-high resolution spectral domain polarization sensitive optical coherence,"* OPTICS EXPRESS 17-22 (2009)

[12]   Antonia M. Joussen, Thomas W. Gardner, Bernd Kirchhof and Stephen J. Ryan, "*Retinal Vascular disease,*" Springer Verlag (2007)

[13]   Bernhard N. Tillmann, "*Atlas der Anatomie des Menschen,*" Springer Verlag (2010)

[14]   Theodor Heinrich Schiebler*, "Anatomie,*" Springer Verlag (2005)

[15]   Huang XR, *"Polarization properties of the retinal nerve fiber layer,"* Bull Soc Belge Ophtalmol. 2006;(302):71-88.

[17]   R. E. Records, "*Physiology of the human eye and visual system,"* Harper & Row, Hagerstown, Md. (1979)

[18]   Hitzenberger C. K., Götzinger E., Pircher M*., "Birefringence Properties of the Human Cornea measured with polarization sensitive optical coherence tomography,*" Bull. Soc. belge Ophtalmol., 302, 153-168, 2006.

[19]   Antonia Joussen, Thomas W. Gardner (Penn State University College of Medicine), Bernd Kirchof, Steph, *"Retinal Vascular Disease,"* Springer Verlag (2007)

[20]   B. Nuyen, K. Mansouri, R.N. Weinreb, "*Imaging of the Lamina Cribrosa using Swept-Source Optical Coherence Tomography,*" J Current Glau Prac 2012; 6(3): 113-119 (2012)

[21]   P Sathyan, Shilpa, Anitha, *"Optical Coherence Tomography in Glaucoma," Journal of Current Glaucoma Practice,"* January-April 2012; 6(1):1-5

[22]   Sommer A, Katz J, Quigley HA, et al. *"Clinically detectable nerve layer atrophy precedes the onset of glaucomatous field loss,"* Arch Ophthalmol 1991; 109:77-83

[23]   Carol Yim Cheung, Christopher Kai-shun Leung *"A practical Guide for Interpretation of Optical Coherence Tomography Retinal Nerve Fiber Layer Measurement,"* Journal of Current Glaucoma Practice, January-April 2009; 3(1):9-13

[24]   Donald C. Hood1,2,* and Ali S. Raza1 *"Method for comparing visual field defects to local RNFL and RGC damage seen on frequency domain OCT in patients with glaucoma,"* 1 May 2011 / Vol. 2, No. 5 / BIOMEDICAL OPTICS EXPRESS 1097

[25]   R. Leitgeb, R. Michaely, T. Lasser, and S. Sekhar, *"Complex ambiguity-free Fourier domain optical coherence tomography through transverse scanning,"* Opt. Lett. 32, 3453-3455 (2007).

[26]   M. Kraus, B. Potsaid, M. Mayer, R. Bock, B. Baumann, J. Liu, J. Hornegger, and J. Fujimoto, *"Motion correction in optical coherence tomography volumes on a per A-scan basis using orthogonal scan patterns,"* Biomed. Opt. Express 3, 1182-1199 (2012).